Continuous variable response, kinetic gating and connectivity that govern IS topology are perturbed in hyperinsulinemia

Namrata Shukla[1*], Shantanu Kadam[2*], Ranjith Padinhateeri[2#] and Ullas Kolthur-Seetharam[1#]

[1]Department of Biological Sciences, Tata Institute of Fundamental Research, Mumbai, Maharashtra, 400005, India

[2]Department of Biosciences and Bioengineering, Indian Institute of Technology Bombay, Mumbai, Maharashtra 400076, India

*Joint first authors: Namrata Shukla and Shantanu Kadam

Joint corresponding authors: Ranjith Padinhateeri (ranjithp@iitb.ac.in) and Ullas Kolthur-Seetharam (ullas@tifr.res.in)

Abstract

Understanding kinetic control of biological processes is as important as identifying components that constitute pathways. Insulin-signaling (IS) is central for almost all metazoans and its perturbations are associated with various diseases and aging. While temporal phosphorylation changes and kinetic constants have provided some insights, constant or variable parameters that establish and maintain signal topology are poorly understood. Our iterative experimental and mathematical simulation-based approaches reveal novel kinetic parameters that encode concentration and nutrient dependent information. Further, we find that pulsatile fasting insulin rewires IS akin to memory and in anticipation of a fed response. Importantly, selective kinetic gating of signals and maximum connectivity, between metabolic and growth-factor arms under normo-insulinemic states, maintains network topology. In addition to unraveling kinetic constraints that determine cascade architecture, our findings will help in identifying novel therapeutic strategies that conserve coupling between metabolic and growth-factor arms, which is lost in diseases and conditions of hyperinsulinemia.

Introduction

Signaling cascades are essential for regulating cellular processes and decades of work has unraveled molecular and biochemical mechanisms that constitute them. However, kinetic parameters that define emergent properties of signaling networks and therefore predict regulatory nodes are poorly understood. While independent experimental and mathematical approaches have provided valuable insights (Behar et al., 2008; Faro et al., 2017; Kubota et al., 2012; Shinar et al., 2007; Somvanshi et al., 2019; Vinod and Venkatesh, 2009; Wilson et al., 2017), studies that capture dynamics and complexities of signaling architecture vis-à-vis physiological variations in input strengths are far fewer. Not only would these reveal fundamental kinetic considerations that determine signal topology but also inform about reactions/entities that could emerge as therapeutic targets.

Insulin signaling (IS), an evolutionarily conserved mechanism is essential for cellular/organismal metabolism and growth (Boucher et al., 2014; Haeusler et al., 2018; Saltiel and Kahn, 2001). Aberrant IS is associated both causally and consequentially with growth abnormalities, inflammation, accelerated aging and diseases including metabolic disorders and cancer (Arcidiacono et al., 2012; Guo, 2014; Hill and Milner, 1985; Shimobayashi et al., 2018; Shoelson et al., 2006; Vigneri et al., 2020). Genetic perturbations and omics-based studies have elucidated importance of key phosphorylation events in response to insulin stimulation (Humphrey et al., 2015; Krüger et al., 2008; Schmelzle et al., 2006; Yugi et al., 2014). Recent reports have provided crucial insights into physical protein interactomes, temporal changes in phospho-proteome and kinetic constants, viz $T_{1/2}$ and EC_{50} (Kubota et al., 2018; Vinayagam et al., 2016). However, kinetic parameters that govern network properties of IS as a function of normo-insulinemic and hyper-insulinemic states

that could collectively determine physiological and pathophysiological outcomes is still lacking.

Our current understanding largely stems from studies, which have used either supra-physiological or static concentrations of insulin. It is important to note that circulating insulin concentrations vary drastically from being low/pulsatile to high/biphasic in fasted and fed states respectively (Krishnan et al., 2018; Lu et al., 2012; Pørksen, 2002; Vander Haar et al., 2007). Moreover, hyper-insulinemia is associated with metabolic disorders such as diabetes and obesity (Menge et al., 2011; Satin et al., 2015; Schmelzle et al., 2006). These are key considerations since kinetic criteria that either encode fasted-to-fed transitions or drive pathological manifestations of IS are unknown. Furthermore, IS can be broadly divided into metabolic and growth factor arms (Mendoza et al., 2011; Petersen and Shulman, 2018). In this regard, while biased signaling is implicated in diseases, if/how the flow of information is stratified and maintained remains to be unraveled.

Mathematical approaches to model cellular signaling have gained traction in the recent past to understand the dynamics and also to provide predictive parameters that define topology of signaling network (Cedersund et al., 2008; Dalle Pezze et al., 2016; Di Camillo et al., 2016; Sedaghat et al., 2002; Sonntag et al., 2012). Earlier such attempts to determine kinetics of insulin signaling have largely employed “averaged” measures to define the behavior of the system (Kubota et al., 2018). Importantly, given the fluctuations in insulin levels and inherent noise in signaling, there are no reports that have computed kinetic parameters, which capture emergent properties of IS. Specifically, while there have been simulation based approaches to define dose-to-duration effects and kinetic insulation

on synthetic signaling networks (Behar et al., 2007), such principles have not been applied to complex cascades such as insulin signaling.

In this regard, our current study addresses how connectedness among signaling components as well as overall network topology is maintained under physiological concentrations of insulin. We further highlight the concentration dependency of barriers in the signaling cascade which maintain hierarchy. Additionally, our study puts emphasis on the importance of dynamic range and pulsatility in signaling which generates memory as well as couples the metabolic and growth factor arms.

Results

Distinct kinetics of signaling in response to physiological and non-physiological concentrations of insulin

Although previous reports have attempted to elucidate dynamics of insulin signaling, kinetic parameters that define signaling architecture in response to physiologically relevant insulin concentrations remain to be unraveled. This is particularly important since circulating concentrations of insulin vary between 0.1 nM and 1.0 nM during normal fed-fast cycles. Moreover, insulin signaling achieves both nutrient uptake and its utilization via anabolic processes, whose perturbations are associated with diseases and accelerated aging. Thus, we wanted to assess the kinetics of signaling through nodal kinases in the cascade, which govern both the metabolic and growth factor arms (Figure 1A). Given the importance of liver in modulation of insulin action and integration of whole-body physiology, we employed primary hepatocytes. Towards this, primary hepatocytes isolated from mice livers were

93 treated with different concentrations of insulin as described in Figure 1B. Our paradigm
94 ensured that the kinetic evaluation did not have any bearing from either residual signals or
95 nutrient inputs alone, as illustrated in Figure 1B and Figure 1- figure supplement 1, A-D.

96 As reported by others (Borisov et al., 2009; Kubota et al., 2012; Kubota et al., 2018;
97 Noguchi et al., 2013) insulin treatment led to a rapid activation of downstream signaling and
98 was consistent with a fed response (Figure 1C-E, Figure 1- figure supplement 1E-F and Figure
99 1- figure supplement 2A-B). Expectedly, overall signal intensities (i.e. area under the curve:
100 AUC), for all the phosphorylation events scored in our assay, were positively correlated with
101 insulin concentration (Figure 1- figure supplement 2C). We define true discovery rate as a
102 statistical measure to compare changes in phosphorylations across time and insulin
103 concentrations. This parameter further validates the statistical robustness of our
104 measurements (Figure 1- figure supplement 2D). It was striking to see that the kinetic
105 behavior of nodal kinases in the cascade, AKT and ERK, was markedly different (Figure 1D-E,
106 Figure 1- figure supplement 1E-F, 2A-B and 3C), which has not been highlighted in any of the
107 previous studies. Importantly, we observe non-linear and non-monotonic association of
108 signal intensities w.r.t insulin concentrations, across the cascade, both in terms of extent of
109 phosphorylation and temporal behavior.

110 For example, activation-inactivation kinetics was starkly different for AKT (T^{308} and
111 S^{473}) and ERK. In addition to this, while the final intensity of AKT phosphorylation
112 approached baseline by 120 minutes, ERK phosphorylation showed a distinct second wave
113 of activation (Figure 1D-E, Figure 1- figure supplement 1E-F, 2A-B and 3C). Similarly, we
114 found that initial induction of phosphorylation of GSK3β and S6K was phase delayed in
115 response to 0.1 nM and 1.0 nM insulin treatments and continued to remain elevated long

after phosphorylation on AKT started to extinguish (Figure 1- figure supplement 1E-F, 2A-B and 3A-B).

Further, on comparing both fed and fasted insulin concentrations, it was apparent that maximal phosphorylation and its sustenance varied drastically for nodal kinase AKT, as can be seen in Figure 1D-E. These clearly indicated that insulin-dependent programming of signaling kinetics was distinct and prompted us to investigate the kinetic parameters that defined this behavior. We adopted an iterative experimental-cum-mathematical approach to gain further insights.

Mathematical modelling of signaling kinetics and predictive assessment of key phosphorylation-dephosphorylation dynamics

Based on our experimental results, we modeled the signaling cascade using mathematical methods with an aim to extract kinetic parameters that define the network. We considered the insulin signaling network as a set of coupled biochemical reactions and used ordinary differential equations (ODE) to describe the system (Aoki et al., 2013; Arkun, 2016; Borisov et al., 2009; Dalle Pezze et al., 2016; Dalle Pezze et al., 2012; Di Camillo et al., 2016; Ho et al., 2015; Huang et al., 2014; Kubota et al., 2012; Kubota et al., 2018; Noguchi et al., 2013; Sedaghat et al., 2002; Zhao et al., 2017). Importantly, we set out to not only test the robustness of our mathematical simulation using experimental results, but also predict the behavior of components that were not measured experimentally.

As shown in Figure 1F-1G and Figure 1 – figure supplement 3D-F, the simulation results for $pAKT^{T308}$, $pAKT^{S73}$, $pGSK3\beta^{S9}$, $pS6K^{T389}$ and $pERK^{T202/Y204}$ were consistent and nearly overlapping with the experimental data, across insulin concentrations. Next, using

experimentally optimized parameters as input, we simulated the phosphorylation dynamics of insulin receptor (IR), mTORC1 and mTORC2 (Figure 1 – figure supplement 3G).

While downstream components scaled with insulin concentration, the most upstream event of insulin receptor phosphorylation was rapid and transient. Intriguingly, kinetics of mTORC1 and mTORC2 were starkly different (Figure 1 – figure supplement 3G). Moreover, even though mTORC2 is not directly downstream to IR, we found their responsivity to be similar qualitatively. To our best knowledge this is one of the first attempts that delineates temporal variations in activation of mTOR complexes. Given that mTORC2 is the primary kinase for S^{473} phosphorylation, the discordant dynamics of mTORC2 phosphorylation and $pAKT^{S473}$ predicts additional regulatory steps in controlling activation of AKT (Figure 1D and Figure 1 – figure supplement 3G).

We also used stochastic simulations to provide an alternative approach to validate our mathematical predictions, which qualitatively resembled the deterministic approach for quantities as described in Figure 1H. In addition to predicting the response at a population level, this allowed us to determine the fluctuations in the system and compare it with signaling topology (see below).

In order to score the robustness of our simulation data, we computed the z-score for all components assessed in the signaling cascade across concentrations (Figure 1I). It is important to note that our iterative toggling between computational and experimental determination of phosphorylation gave highly consistent results. Further, low values of false discovery rate calculations suggested statistical similarity between simulation and experimental data (Figure 1 – figure supplement 3H).

AKT-dependent responsivity to insulin is determined by phosphorylation at S^{473}

Several reports have highlighted the necessity of dual phosphorylation of AKT at T^{308} and S^{473} for its activity (Bertuzzi et al., 2016; Manning and Toker, 2017; Sarbassov et al., 2005). Despite this it is still unclear as to which of these provides the gain in terms of signal strength and responds to dynamic changes in insulin concentrations. Thus, we computed percentage gain in signal against physiological insulin concentrations of 0.1 and 1 nM for $pAKT^{T308}$ and $pAKT^{S473}$ (Figure 2A). $pAKT^{T308}$, that is directly downstream to insulin receptor, showed comparable activation with no change in peak intensity across fasted and fed insulin concentrations. On the contrary, $pAKT^{S473}$, which is indirectly dependent on insulin via mTORC2, displayed dose responsiveness to insulin concentrations and variable kinetics (Figure 2A-B). This finding posits that while $pAKT^{T308}$ may serve to prime the signaling, $pAKT^{S473}$ determines the extent of overall activation in response to fed insulin doses.

Non-concordant peak and final amplitudes define dynamic range of nodal signaling events

Threshold of activation and dynamic range are key determinants of responsivity in signaling, especially when the inputs are dynamic, as in the case of IS. We wanted to determine (a) the relationship between peak intensity and decay kinetics, and (b) dynamic range and threshold activation, which collectively dictate the physiological output. Phase diagram depicting peak amplitudes and decay time of phosphorylation events highlighted non-concordance between these for AKT but not for pGSK3β and pS6K (Figure 2B).

Most experimental approaches in the past have assayed for signaling in response to very high inputs, which is rarely physiological. Such deterministic evaluation of signaling also masks threshold kinetics, which is critical to encode biological response. Therefore, on simulating the phosphorylation events across concentrations from 0.1 nM to 1.0 nM, we found disparate dynamic ranges for activation (Figure 2C). While AKT phosphorylations

(both at S^{473} and T^{308}) displayed large and nearly overlapping dynamic range, $pS6K^{T389}$ and $pGSK3\beta^{S9}$ reach saturation at lower concentrations of insulin (Figure 2C-D). Taken together with dose-dependency of $pAKT^{S473}$ (Figure 2A), these results clearly suggest that while dual phosphorylation of AKT is important for its activity, $pAKT^{S473}$ is a crucial regulatory node during fast to fed transitions.

Since our simulations predicted non-saturation dynamics for $pAKT^{S473}$, we wanted to experimentally verify if this was indeed the case. We specifically chose 0.3 nM and 0.6 nM, as the response is linear at 0.3 nM and begins to plateau at 0.6 nM insulin. As shown in Figure 2 – figure supplement 1A-B, our experimental results were consistent with the mathematical predictions and clearly indicated that $pAKT^{S473}$ indeed displayed a large dynamic range to insulin inputs.

Interestingly, the variability in dynamic range was independent of the final amplitudes (Figure 2 – figure supplement 1C) as it returned to the same level at 120min, for all the phosphorylations assessed. Such non-concordance between peak and final amplitudes across signaling components raised the exciting possibility of existence of (a) kinetic insulation of signals and (b) memory of fasted insulin inputs, which together would define the fed insulin response.

Diverse insulin inputs generate differential kinetic gates and signal noise

In a multi-component and multi-step signaling cascade, such as insulin signaling, it is important to determine parameters that (a) define the topology or the information flow through the network and (b) those that maintain robustness of the network/topology. Kinetic insulation has been proposed as one of the key determinants of non-uniform flow of information. Although inferred by mathematical approaches (Behar et al., 2007; Behar et al.,

2008) on a synthetic cellular signaling cascade, it has not been applied to a dynamic physiological system such as insulin signaling.

In this context, we used our experimental data and mathematical simulations (methods) to deduce kinetic gates that define topology of insulin signaling. To reveal kinetic gating/insulation we computed rate constants for phosphorylation events, which included known feed-forward and feed-back regulatory inputs (Figure 3- figure supplementary 1A-B). A simple-minded assumption was that very high or low ratios of K_{ON}/K_{OFF} would constitute kinetic "gates" that determined differential flow of signals. A phase diagram of K_{ON}/K_{OFF} ratios for key phosphorylation events is depicted in Figure 3A, wherein we applied $10^{+/-1}$ as the threshold or barrier.

Interestingly, at insulin concentration of 1 nM, which mimics a physiologically fed state, most reactions were not gated and were unlike the response to very low and very high insulin concentrations. For example, AKT activation (reaction 5) was more sensitive at lower insulin concentration i.e. there was a negative barrier while at 1 and 10 nM there was no gating. On the contrary, activation of GSK3β (reaction 10) was highly gated at both very low and very high insulin concentrations. We also observed a peculiar pattern between nodal priming events {viz. reactions 1 (Ins+IR ⇄ p1IRC), 6 (ppAKT+mTORC1 ⇄ ppAKT+pmTORC1), 10 (ppAKT+GSK3β ⇄ ppAKT+pGSK3β) and 11 (p1IRC+Raf ⇄ p1IRC+Raf*)} and their effector or downstream phosphorylations {reactions 4 (p1IRC+$pAKT^{S473}$ ⇄ p1IRC+ppAKT), 5 (pmTORC2+$pAKT^{T308}$ ⇄ pmTORC2+ppAKT) and 12 (Raf*+ERK ⇄ Raf*+ppERK)} vis-à-vis kinetic gates specifically at 0.1 nM. Together, it was striking to see that strong negative and positive barriers were differentially associated with metabolic and growth factor arms of the cascade in response to fasted, fed and supra-physiological insulin inputs.

Since phosphorylation of AKT is one of the central events that is used as surrogate for IS, and given the differential dynamics of $pAKT^{T308}$ and $pAKT^{S473}$, we wanted to assess their individual contributions to functional flexibility. We went ahead to compute noise in their signaling (fluctuations on mathematically determined concentrations; see methods). This is relevant as often noise in biology becomes important for mounting a robust response in addition to generating functional heterogeneity and flexibility especially in a dynamic system like IS (Bowsher et al., 2013; Silva-Rocha and de Lorenzo, 2010; Thattai and Van Oudenaarden, 2001). As shown in Figure 3B, we observed that lower concentrations of insulin generate more noise than higher concentration across time points assessed. While being in general agreement with similar measurements of other biological parameters, this also indicated that the differential phosphorylation dynamics of AKT^{T308} and AKT^{S473} were independent of noise. In summary, the results described in this section clearly indicated that differential insulin inputs mounted diverse kinetic responses, which together could possibly exert a control over topology of the cascade.

Robust IS topology is achieved at physiological insulin inputs

Topology and robustness of a network is governed by the degree of connectedness among the network components and is defined by how correlated their responses are. Therefore, we set out to ask if supra-/physiological inputs of insulin had any bearing on signaling topology.

Computing Pearson coefficient across time for different insulin concentrations gave us a correlation matrix comparing each phosphorylation event with the other (Figure 3C). We observed that maximal correlations are lost under supraphysiological concentration of 10 nM compared to physiological concentrations of insulin.

Next, we checked if high degree of correlation in response to fed and fasted insulin inputs had any impact on the topology of the network. For a maximally connected network of "n" nodes the maximum number of edges would be n(n-1)/2; while the minimum number of edges would be (n-1). Applying this to a five-component system (as in our case) should give a maximum of 10 connections, although 34 undirected non-isomorphic graphs can be realized. We found that when 5 nodes (vertices) corresponding to $pAKT^{S473}$, $pAKT^{T308}$, $pS6K^{T389}$, $pGSK3\beta^{S9}$, $pERK^{T202/Y204}$ were used, maximum connectivity was obtained at physiological concentrations of insulin (at 0.1 nM and 1.0 nM) (Figure 3D and Figure 3 - figure supplement 1C). Distinctively the network broke at 10 nM insulin and the node corresponding to pERK was disconnected, which indicated decoupling of the metabolic and growth factor arms with possible pathophysiological implications.

To understand which of the nodes control topology of the network, we substituted individual nodes of 0.1 and 1 nM insulin network with that of 10 nM while keeping the rest unperturbed. Perturbation of every component changed network properties with a reduction in both the number of nodes as well as edges (Figure 3E and Figure 3- figure supplement 2 and 3A-D). Interestingly, while perturbation of $pAKT^{S473}$ caused disappearance of some edges, perturbation of $pAKT^{T308}$ completely broke the network, bringing the connections down from 6 to 2 (Figure 3E and F).

Pulsatile fasting insulin rewires response to fed insulin inputs akin to memory

Uniquely, insulin is released in a pulsatile manner during a fasted state (O'Meara et al., 1993; O'Rahilly et al., 1988), which is followed by a biphasic secretion in response to fed nutrient inputs. As mentioned earlier, while most studies on signaling dynamics have used high concentrations of insulin, there are no reports that have investigated kinetics and

topology vis-à-vis pulsatile fasted insulin inputs. Moreover, if/how a fasted input shapes signaling architecture in a fed state has not been addressed, thus far.

To this end, we pulsed hepatocytes with 0.1 nM insulin and then subsequently treated with 1 nM insulin as a proxy to physiological dynamics of fasted and fed insulin inputs, as indicated (Figure 4A). Surprisingly, we found that there was neither sustenance nor an enhanced response to consequent insulin pulses, for pAKT$^{T308 \text{ and } S473}$ (Figure 4B-C and Figure 4 – figure supplement A), which was unanticipated. This striking loss of pAKT signal by the end of 4th pulse (at 0') was distinct from a continuous step treatment as described earlier (Figure 1D-E) and indicated a memory of signaling. This behavior was not seen for pERK (Figure 4D and Figure 4 – figure supplement B). Interestingly, pAKT levels reached a new baseline following pulsatile insulin stimulation (Figure 4B-C). This new reset point of pAKT also changed the kinetics following 1 nM insulin treatment, which was distinct from pERK, pGSK3β and pS6K phosphorylation (Figure 4D and Figure 4- figure supplement 1B-F). These results clearly indicated that fasted insulin pulses created a memory to possibly enhance the response to fed insulin inputs. In support of this hypothesis, network analyses of this pulsatile adapted fed IS showed more connectedness (as compared to 1 nM alone) (Figure 4E and Figure 4 – figure supplement 1G). Additionally, we also looked at the transcription of genes downstream of a pulsatile adapted system. In line with the signaling data, the transcription of target genes was also more robust post adaptation (Figure 4F).

Repeated stimulation by fed insulin abrogates the synergy between the metabolic and mitogenic arms of signaling

Although continuous exposure to higher levels of circulating insulin is known to cause resistance and thus metabolic diseases, the kinetic basis for such a signalling has not

been investigated. In this context, we repeat stimulated hepatocytes with 1 nM insulin, as indicated in Figure 5A. This led to an anomalous response vis-à-vis both metabolic (pAKT) and mitogenic (pERK) arms of signalling. While pAKT levels decreased drastically, amplitude of pERK peaks increased following repeated stimulation (RS1 and 2) of fed insulin inputs (Figure 5B-D and Figure 5- figure supplement 1A). Network analysis following this paradigm showed complete loss of connections among signalling components (Figure 5E and Figure 5- figure supplement 1D). This was also apparent with the dynamics of pGSK3b and pS6K, which remain upregulated despite a downregulation in AKT signalling (Figure 5- figure supplement 1A-C). Interestingly, repeated stimulation of fed insulin also led to a loss in transcriptional robustness (Figure 5F).

Discussion

Coupling nutrient inputs to cellular metabolism, survival and growth is intrinsically dependent upon Insulin signalling (IS). Hypo- and hyper- activation of IS leads to various patho-physiologies including diabetes, accelerated aging and cancer, which are attributed to under- or over-phosphorylation of certain IS components (Arcidiacono et al., 2012; Guo, 2014; Hill and Milner, 1985; Shimobayashi et al., 2018; Shoelson et al., 2006; Vigneri et al., 2020). Despite this our ability to tweak the cascade to restore balance between metabolic and mitogenic arms has been limited by paucity of information vis-à-vis parameters that govern network topology. In this study, using mathematical and experimental approaches, we have provided fundamental insights into kinetic parameters that dictate emergent properties of IS and its architecture, under various physiological contexts.

Given the contribution of the liver in maintaining whole organismal physiology and insulin action, including development of metabolic diseases, we have specifically utilized primary hepatocytes for deciphering kinetic constants or determinants that exert a control over IS. It should be noted that while it is nearly impossible to recreate paradigms that mirror in-vivo conditions, we have employed insulin treatment regimens that mimic normo- and hyper-insulinemic states. Moreover, in-vivo complexity of insulin-dependent endocrine and paracrine networks would severely confound attempts to unveil kinetic determinants. Our study has revealed novel insights into kinetic control of insulin signalling and also provides a model to capture such parameters in other cells or tissue types, including by coupling other endocrine/paracrine inputs.

While genetic, biochemical and pharmacological perturbations have described inter-dependence of IS phosphorylation events, recent phospho-proteomic analyses have unravelled their temporal behaviour. However, the extent to which phosphorylation dynamics encode information as a function of insulin concentration and/or time is still unclear. For example, even though hypo-/hyper-phosphorylations at T^{308} and S^{473} are considered as proxy markers for AKT activity and signalling downstream to insulin, whether or not their kinetic differentials contribute to insulin responsiveness remains unknown. Here, we surprisingly found that while the gain and kinetics of pT^{308} (IR/PDK1 dependent) was independent of input strength, phosphorylation of S^{473} (downstream to mTORC2) correlated with change in ligand concentration and displayed highest gain in signal in response to a fed insulin input.

Further, in contrast to net gain in specific phosphorylation, dynamic range, which is undetermined for many signalling networks including IS, has been proposed to be a better

predictor of cellular response. In this regard, our simulation and experimental data together revealed a large dynamic range for $pAKT^{T308}$ and $pAKT^{S473}$, which was nearly overlapping. This suggests that both these phosphorylations are equally responsive to relative change in insulin inputs vis-à-vis physiological fed-fast cycles wherein circulating concentrations vary between 0.1nM and 1.0 nM. Surprisingly, we also found that pT^{308} is a key determinant of network topology, which also highlights distinct properties of AKT phosphorylations in contributing to flow of information. Taken together these also raise the possibility of pT^{308} and pS^{473} acting as low pass and high pass filters with former being a permissive cue, which was hitherto unknown.

Noise in biology is generally regarded to be beneficial for regulating functional flexibility and has been well studied in the context of gene transcription. Given limited knowledge in this regard for signalling cascades (especially for IS), we checked for input versus variance in signal response for the nodal kinase AKT. It was interesting to note that noise in signaling was apparent at physiological concentrations of insulin (0.1-1 nM) while it was substantially diminished in hyper-insulinemic regimes. This hinted towards reduced flexibility in signaling under hyper-insulinemic states.

Signal stratification is crucial for sustenance of downstream information even upon input extinction. We discovered that signals are stratified with differential gating, in an insulin concentration dependent manner, with kinetic barriers/gates emerging at both low and hyper-insulinemic concentrations. These bring to the fore the need to address mechanisms that contribute to these kinetic barriers by affecting K_{ON}/K_{OFF} ratios of phosphorylation events, in the future. We propose such components would be very

366 attractive candidates for therapeutic interventions to regulate insulin signalling and
367 maintain network properties.

368 In addition to differential kinetic gating, connectedness between signalling
369 components determines topology of the network. Despite several studies on signalling
370 cascades across biological systems, little is known about if/how these parameters contribute
371 to topology, except in cases where simulations have been carried out for artificial signalling
372 systems. Our iterative experimental-simulation approach has revealed that maximum
373 connectivity between the signalling nodes, which is often used as a measure of network
374 robustness, is achieved at physiological concentrations of insulin. Conversely, the network
375 breaks at hyper-insulinemic states. Importantly, we also underscore the significance of each
376 of the phosphorylations in maintaining the robustness of the topology under normo-
377 insulinemic states.

378 Others and we have found that metabolic cues under fasting conditions elicit
379 anticipatory molecular mechanisms to mount an efficient fed response (Chattopadhyay et
380 al., 2020; Maniyadath et al., 2019; Shaw et al., 2020). Given that fasting insulin (0.1nM) is
381 pulsatile with a frequency of 10-15min, our findings have shown that this rewires fed IS
382 dynamics. Strikingly, we found that coupling low pulsatile inputs with 1.0nM insulin
383 stimulation, as in the case of fasted to fed transition, enhanced net gain in phosphorylation
384 of some (pAKT$^{T308 \text{ and } S473}$ and pGSK3β^{S9}) but not all components, akin to memory or
385 anticipation. Conversely, insulin resistance is associated with repeated insulin/nutrient
386 inputs and hyperinsulinemia. Our study also describes kinetic changes in IS dynamics, which
387 can be either causal or consequential to reduced sensitivity under these conditions. Notably,
388 we found that repeated stimulation with fed concentrations of insulin damped the AKT

response while upregulating pERK indicating a disbalance between metabolic and mitogenic arms. This is important because overactivation of either metabolic and/or the mitogenic arm has been described in literature as a driver of metabolic diseases and cancer (Altomare and Testa, 2005; Burotto et al., 2014; De Luca et al., 2012; Shaw and Cantley, 2006). Here, we would like to specifically highlight that the signaling network is most robust in response to fed insulin inputs, which is pulse primed by fasting insulin. Our findings posit that repeated and/or high insulin inputs, including in a clinical setting could lead to perturbed networks with possible pathological manifestations.

In conclusion, our results unravel hitherto unknown kinetic constraints that exert control over components of insulin signaling. Notably, we illustrate that these kinetic parameters are intrinsically linked to insulin concentrations as in normo- and hyper-insulinemic states. Given that a discordant signal flow between metabolic and growth-factor arms is associated with diseases, our findings provide fundamental insights into factors that govern this coupling. Our study also raises the possibility of impaired biological outputs in the context of therapeutic interventions using insulin, which have been largely guided by glycemic control. We highlight the importance of discovering novel regulatory parameters/nodes to complete our understanding of signaling cascades under both normal and pathological conditions.

Materials and Methods

Animals

2.5-3 month old C57BL/6NCr mice were used for hepatocyte isolation. The animals were housed under standard animal house conditions with a 12h day and night cycle. All

412 procedures were done in accordance with the institute animal ethics committee (IAEC)
413 guidelines.

414 **Primary Hepatocyte Isolation and culture**

415 Male mice were sedated by giving intraperitoneal Thiopentone (Neon Laboratories Ltd.,
416 Mumbai, India) injection. Liver perfusion was done via inferior vena cava using 30mL Hank's
417 Balanced Salt Solution, HBSS (5.33 mM Potassium chloride, 0.44 mM KH_2PO_4, 4.16 mM
418 $NaHCO_3$, 137.93 mM NaCl, 0.338 mM Na_2HPO_4, pH 7.4) containing 5.5 mM Glucose (Sigma-
419 Aldrich G8769), 25mM HEPES pH 7.2 (USB 16926) and 100mM EGTA (Sigma-Aldrich E3889).
420 Hepatic portal vein was cut at one end in order to drain out the blood. Perfused liver was
421 digested using collagenase (Sigma-Aldrich C5138) dissolved in 50mL Digestion medium
422 {DMEM-LG (Sigma-Aldrich D5523), 15mM HEPES pH 7.2 (USB 16926) and Anti-Anti (Sigma-
423 Aldrich A5955)}. Liver was cut into pieces, minced and incubated in Digestion Medium for
424 5min. The cells were strained using a 70µm cell strainer and centrifuged at 50G for 5min.
425 Cell pellet was washed twice with DMEM-HG (Sigma-Aldrich D7777) and re-suspended in
426 DMEM-HG containing 10% FBS (Gibco 16000044) for plating. Trypan blue staining was done
427 to check cell viability. Cells were plated at a density of 7.5 x 10^5 cells/60mm plate in collagen
428 (Sigma-Aldrich C3867) coated plates (5µg/cm^2). Cells were grown at 37^{o}C and 5% CO_2.
429 Medium was changed 6h post plating to ensure proper cell adherence.

430 **Insulin Treatments**

431 24h post plating, the hepatocyte medium was changed to 5% FBS containing DMEM-HG for
432 11h. Medium was changed to Earle's Balanced Salt Solution, EBSS (Sigma-Aldrich E2888) for
433 6h to get a baseline (0m) signal. For one step insulin stimulation experiments, 0.1-100nM
434 Insulin (Sigma-Aldrich I0516) in DMEM-HG was added to the hepatocytes and cells were

435 collected at time points as described in the results. For pulsatile insulin treatments and
436 repeated insulin stimulation, paradigm modifications are mentioned in Figure 4A and 5A.
437 Every media change was preceded with a PBS wash to remove residual contamination.

438 **Protein Lysate Preparation**

439 Hepatocytes were lysed in RIPA lysis buffer (50mM Tris pH 8.0, 150mM NaCl, 0.1% SDS,
440 0.5% Sodium deoxycholate, 1% Triton X-100, 0.1% SDS, 1 mM PMSF, Protease inhibitor
441 cocktail and phosphatase inhibitor- Sigma-Roche 4906845001) for 30min. Cell debris were
442 pelleted by centrifuging at 12,000rpm at 4^{o}C for 15min. BCA assay kit (Sigma-Aldrich 9643)
443 was used for protein estimation. Protein samples were boiled in a loading buffer (8% SDS,
444 40% glycerol, 240mM Tris pH 6.8, 0.2g bromophenol blue and 3.05g DTT) and stored at -
445 20^{o}C.

446 **Western Blotting**

447 50µg of protein was loaded onto SDS gel and run at 90V for stacking and 120V for resolving.
448 Gels were transferred to ethanol activated PVDF membranes (Merck IPVH00010-IN) at 90V
449 for 2h. Protein blotted membranes were blocked in 5% skimmed milk. Blots were cut
450 according to protein molecular weight as indicated by pre-stained ladder (Abcam ab116028)
451 and incubated overnight with the respective primary antibodies: AKT (CST 9272), pAKT^{S473}
452 (CST 4060), pAKT^{T308} (CST 13038), ERK1/2 (CST 4695), pERK1/2$^{T202/Y204}$ (CST 4376), GSK3β
453 (CST 12456), pGSK3β^{S9} (CST 5558), pS6K^{T389} (CST 9234) and S6K (CST 2708). Blots were
454 incubated with appropriate secondary antibodies (Anti-Rabbit IgG- Peroxidase Sigma-Aldrich
455 A0545 and Anti-Mouse IgG- Peroxidase Sigma-Aldrich A9044) and imaged using GE
456 Amersham Imager 600.

457 **RNA extraction, cDNA synthesis and RT-PCR**

458 RNA extraction, cDNA synthesis and real time PCR was performed as per manufacturer's
459 instructions. Briefly, total RNA was extracted from hepatocytes using TRIzol reagent
460 (Ambion-Invitrogen 15596-018) and 1ug of RNA was used to make cDNA using SuperScript
461 IV RT Kit (Invitrogen 18090010). Quantitative PCR was done using KAPA SYBR® FAST
462 Universal 2X qPCR Master Mix (KAPA Biosystems KK4601) and LightCycler 96 instrument
463 (Roche). The list of primers used are depicted in the table below:

Gene Name	Forward Primer	Reverse Primer
FOS	GTCAACACACAGGACTTTTG	AGATAGCTGCTCTACTTTCA
EGR1	CACTGACATTTTTCCTGAGC	TAGTGGATAGTGGAGTGAGC
c-JUN	TACACGACTACAAACTCCTG	GGGGGTAAAAGTACTGTCCC
SRF	GAGCCAGATCTCACCTACCAG	CTGACACTAGCAGACACTG
ChREBP	CATCTCCAGCCTCGTCTTC	CTTGGTCTTAGGGTCTTCAGG
LPK	CTTGCTCTACCGTGAGCCTC	ACCACAATCACCAGATCACC
GLUT2	GTCACTATGCTCTGGTCTCTG	CAAGAGGGCTCCAGTCAATG
PEPCK	GTTCCCAGGGTGCATGAAAG	AGGGCGAGTCTGTCAGTTCAA
PPARG	AGGGCGATCTTGACAGGAAA	TCTCCCATCATTAAGGAATTCATG
SCD1	CTGACCTGAAAGCCGAGAAG	AGAAGGTGCTAACGAACAGG
ACC	AAGGCTATGTGAAGGATGTGG	CTGTCTGAAGAGGTTAGGGAAG
CPT1A	ACTCCGCTCGCTCATTCCG	CACACCCACCACCACGATAA
GCK	CAACTGGACCAAGGGCTTCAA	TGTGGCCACCGTGTCATTC
GLUT1	CCCCCCAGAAGGTTATTGAG	CCAACAGGTTCATCATCAGC

LDHA	ACAGTTGTTGGGGTTGGTGC	CGCAGTTACACAGTAGTCTTTG
Aldolase A	GCTATCAACAAGTGCCCCCT	GCTGCCTTCAGGTTCTCCTT
DGAT2	CTGTGCTCTACTTCACCTGGCT	CTGGATGGGAAAGTAGTCTCGG
ACLY	AGGAAGTGCCACCTCCAACAGT	CGCTCATCACAGATGCTGGTCA
LXRa	CTGAAGCGGCAAGAAGAGGA	CTGTGGCAGGACTTGAGGAG
18S	TTTCGAGGCCCTGTAATTGG	CCCAAGATCCAACTACGAGC

464

465 **Data Processing**

466 Intensity measurements from the blots were done using Fiji-ImageJ software with
467 corresponding background correction.

468 **Network Analysis**

469 Network construction, visualization and analysis was performed using Cytoscape (version
470 3.7.2) using Pearson correlation data obtained from GraphPad Prism (version 8).

471 **Quantitation and Statistical Analysis**

472 Data are expressed as means ± standard error of means (SEM). Statistical analyses were
473 performed using Microsoft Excel (2013) and GraphPad Prism (version 8). Statistical
474 significance was determined by the Student's t test. A value of $p \leq 0.05$ was considered
475 statistically significant. *$p \leq 0.05$; **$p \leq 0.01$; ***$p \leq 0.001$.

476 **Calculation of z-score and true/false discovery rate (TDR/FDR)**

477 Z-score was calculated by computing the difference between experimental and simulation
478 for each time point. Like in a paired t-test or z-test, we computed the z-value by calculating
479 the mean of the differences and dividing by the standard deviation. If $z < 1.96$, the null

hypothesis — that the experimental and simulation mean values are statistically the same was accepted. For computing FDR, difference between experimental and simulation data was divided by standard errors for different insulin concentrations and z-values were calculated. $z > 1.96$ it is was rejected and counted as false discovery and further averaged to obtain the false discovery rate. For two different insulin concentrations, we define a true discovery rate, which is calculated by taking difference between mean values and dividing by root of sum of square of standard errors. If $z > 1.96$, the null hypothesis is rejected and counted as true discovery and averaged to obtain the true discovery rate.

Estimation of Parameters for Deterministic Simulations

The proposed pathway of insulin signaling is modelled in terms of ordinary differential equations by using mass action kinetics (Alon, 2019; Klipp et al., 2016) . The set of equations that is used to define the insulin signaling network, which is considered both single (denoted by 'p') and double phosphorylation (denoted by 'pp') events and feedback inhibitions, are depicted in Figure S3. We have solved these sets of ordinary differential equations using MatLab version R2015b, Math Works. The parameters of the model (rate constants of reactions and initial amounts of proteins) were decided such that the model fitted with the experimental data. The constrained nonlinear optimization technique was implemented using the 'fmincon' function in MatLab to provide parameters that fit best with the available data. That is, we optimized (minimized) the function:

$$S=\sum i,j[E(i,j)-S(i,j)]^2$$

where, $E(i, j)$ and $S(i, j)$ are the experimental and simulation data, respectively, for the i^{th} protein component at j^{th} time point. The function essentially measures the deviation of the experimental data, and is defined as the sum of the squares of the differences between

503 experimental measurements and simulated trajectories over all the measured proteins. We
504 took 100 independent runs of the program to estimate these parameters. We choose the
505 parameters that correspond to a minimum objective function value resulting in a good fit.
506 All parameters were obtained for different insulin concentrations.

507 **Parameters used in Stochastic Simulations**

508 This reaction network is simulated by using the kinetic Monte Carlo based Doob-Gillespie
509 Algorithm (Doob, 1942, 1945; Gillespie, 1976, 1977). The rate constants of respective
510 reactions are taken from the deterministic model proposed earlier. These rate constants are
511 converted to stochastic framework by using appropriate conversion factors. For
512 unimolecular reactions, the deterministic rate constants (k_j) and stochastic rate constants
513 (c_j) are numerically equal. For bimolecular reactions, when two reactants correspond to
514 different proteins, the stochastic rate constants (c_j) are equal to k_j/V, where V is the system
515 volume (Gillespie, 1976, 1977). The concentration of proteins from a deterministic regime
516 are converted to the number of proteins per cell by multiplying the concentrations by $N_a \times$
517 V, where N_a is the Avogadro's number and $V = 3\times10^{-12}$ liters is the estimated volume of a
518 cell. During the simulation, in any particular iteration from a given reaction network a single
519 bio-chemical reaction and the subsequent time step is chosen randomly. In this way, a single
520 stochastic trajectory is generated by running the simulation for a desired time. Further,
521 many more realizations of this trajectory are generated to compute different moments (e.g.
522 mean, standard deviation) of the probability distributions.

523 Estimation of Insulin Molecules: To estimate the number of insulin molecules from
524 concentration, we assumed a spherical shell (around the cell membrane) of 20nm size and
525 computed the corresponding volume. Assuming a spherical cell of volume $V = 3\times10^{-12}$ litres

the volume of this shell is $\Delta V = 0.0199\times10^{-12}$ litres. Hence the number of insulin molecules are estimated by calculating $N_a \times \Delta V$, where N_a is the Avogadro's number.

(i) For 0.1 nM Insulin: the number of insulin molecules are found to be

1.1985 molecules per spherical shell (1 insulin per spherical shell)

(ii) For 1 nM Insulin: the number of insulin molecules are found to be

11.9857 molecules per spherical shell (12 insulin molecules per spherical shell)

(iii) For 10 nM Insulin: the number of insulin molecules are found to be

119.8577 molecules per spherical shell (120 insulin molecules per spherical shell)

Calculation of decay rate

Decay times are calculated for dynamic protein concentrations measured and simulated in our studies by fitting an exponential function (e^{-kt}) from the time point at which peak intensity is maximum to the final time point at which the intensity falls down.

Calculation of parameters in kinetic gating

The kinetic gating in the signaling cascade is studied by taking the ratio of phosphorylation rate constant (K_{ON}) and the de-phosphorylation rate constant (K_{OFF}) of each biochemical reaction. In case of the degradation reactions, their rate constants are incorporated by averaging with the rate constants of appropriate reactions.

Acknowledgements

We acknowledge Dr. Shital Suryavanshi, Dr. Kalidas Kohale and TIFR-Animal House staff for help with animal breeding and maintenance. This research has been supported by funds to

547 U.K.-S. {DAE-TIFR (Government of India grant - 12P0122), Department of Biotechnology
548 (DBT, India grant BT/PR4972/AGR/36/714/2012) and Swarnajayanti fellowship (DST
549 Government of India grant DST/SJF/LSA-02/2012-13)}, R.P. (DBT, India grant
550 BT/HRD/NBA/39/12/2018-19) and S.K. (Department of Science and Technology, India
551 under Science and Engineering Research Board (SERB) - National Post-doctoral Fellowship
552 (NPDF) with file number: PDF/2017/002502). We also thank the members of UK lab, TIFR for
553 useful discussions and constructive comments.

554 **Competing interests**

555 The authors declare that no competing interests exist.

References

Alon, U. (2019). An introduction to systems biology: design principles of biological circuits (CRC press).

Altomare, D.A., and Testa, J.R. (2005). Perturbations of the AKT signaling pathway in human cancer. Oncogene *24*, 7455-7464.

Aoki, K., Kumagai, Y., Sakurai, A., Komatsu, N., Fujita, Y., Shionyu, C., and Matsuda, M. (2013). Stochastic ERK activation induced by noise and cell-to-cell propagation regulates cell density-dependent proliferation. Molecular cell *52*, 529-540.

Arcidiacono, B., Iiritano, S., Nocera, A., Possidente, K., Nevolo, M.T., Ventura, V., Foti, D., Chiefari, E., and Brunetti, A. (2012). Insulin resistance and cancer risk: an overview of the pathogenetic mechanisms. Experimental diabetes research *2012*.

Arkun, Y. (2016). Dynamic Modeling and Analysis of the Cross-Talk between Insulin/AKT and MAPK/ERK Signaling Pathways. PLoS One *11*, e0149684.

Behar, M., Dohlman, H.G., and Elston, T.C. (2007). Kinetic insulation as an effective mechanism for achieving pathway specificity in intracellular signaling networks. Proceedings of the National Academy of Sciences *104*, 16146-16151.

Behar, M., Hao, N., Dohlman, H.G., and Elston, T.C. (2008). Dose-to-duration encoding and signaling beyond saturation in intracellular signaling networks. PLoS Comput Biol *4*, e1000197.

Bertuzzi, A., Conte, F., Mingrone, G., Papa, F., Salinari, S., and Sinisgalli, C. (2016). Insulin signaling in insulin resistance states and cancer: a modeling analysis. PloS one *11*, e0154415.

577 Borisov, N., Aksamitiene, E., Kiyatkin, A., Legewie, S., Berkhout, J., Maiwald, T.,
578 Kaimachnikov, N.P., Timmer, J., Hoek, J.B., and Kholodenko, B.N. (2009). Systems-level
579 interactions between insulin–EGF networks amplify mitogenic signaling. Molecular systems
580 biology *5*, 256.

581 Boucher, J., Kleinridders, A., and Kahn, C.R. (2014). Insulin receptor signaling in normal and
582 insulin-resistant states. Cold Spring Harbor perspectives in biology *6*, a009191.

583 Bowsher, C.G., Voliotis, M., and Swain, P.S. (2013). The fidelity of dynamic signaling by noisy
584 biomolecular networks. PLoS Comput Biol *9*, e1002965.

585 Burotto, M., Chiou, V.L., Lee, J.M., and Kohn, E.C. (2014). The MAPK pathway across
586 different malignancies: a new perspective. Cancer *120*, 3446-3456.

587 Cedersund, G., Roll, J., Ulfhielm, E., Danielsson, A., Tidefelt, H., and Strålfors, P. (2008).
588 Model-based hypothesis testing of key mechanisms in initial phase of insulin signaling. PLoS
589 computational biology *4*, e1000096.

590 Chattopadhyay, T., Maniyadath, B., Bagul, H.P., Chakraborty, A., Shukla, N., Budnar, S.,
591 Rajendran, A., Shukla, A., Kamat, S.S., and Kolthur-Seetharam, U. (2020). Spatiotemporal
592 gating of SIRT1 functions by O-GlcNAcylation is essential for liver metabolic switching and
593 prevents hyperglycemia. Proceedings of the National Academy of Sciences *117*, 6890-6900.

594 Dalle Pezze, P., Ruf, S., Sonntag, A.G., Langelaar-Makkinje, M., Hall, P., Heberle, A.M., Navas,
595 P.R., Van Eunen, K., Tölle, R.C., and Schwarz, J.J. (2016). A systems study reveals concurrent
596 activation of AMPK and mTOR by amino acids. Nature communications *7*, 1-19.

597 Dalle Pezze, P., Sonntag, A.G., Thien, A., Prentzell, M.T., Gödel, M., Fischer, S., Neumann-
598 Haefelin, E., Huber, T.B., Baumeister, R., and Shanley, D.P. (2012). A dynamic network model

599 of mTOR signaling reveals TSC-independent mTORC2 regulation. Science signaling *5*, ra25-
600 ra25.

601 De Luca, A., Maiello, M.R., D'Alessio, A., Pergameno, M., and Normanno, N. (2012). The
602 RAS/RAF/MEK/ERK and the PI3K/AKT signalling pathways: role in cancer pathogenesis and
603 implications for therapeutic approaches. Expert opinion on therapeutic targets *16*, S17-S27.

604 Di Camillo, B., Carlon, A., Eduati, F., and Toffolo, G.M. (2016). A rule-based model of insulin
605 signalling pathway. BMC systems biology *10*, 38.

606 Doob, J.L. (1942). Topics in the theory of Markoff chains. Transactions of the American
607 Mathematical Society *52*, 37-64.

608 Doob, J.L. (1945). Markoff chains--denumerable case. Transactions of the American
609 Mathematical Society *58*, 455-473.

610 Faro, J., Castro, M., and Molina-París, C. (2017). A unifying mathematical framework for
611 experimental TCR-pMHC kinetic constants. Scientific reports *7*, 46741.

612 Gillespie, D.T. (1976). A general method for numerically simulating the stochastic time
613 evolution of coupled chemical reactions. Journal of computational physics *22*, 403-434.

614 Gillespie, D.T. (1977). Exact stochastic simulation of coupled chemical reactions. The journal
615 of physical chemistry *81*, 2340-2361.

616 Guo, S. (2014). Insulin signaling, resistance, and the metabolic syndrome: insights from
617 mouse models to disease mechanisms. The Journal of endocrinology *220*, T1.

618 Haeusler, R.A., McGraw, T.E., and Accili, D. (2018). Biochemical and cellular properties of
619 insulin receptor signalling. Nature Reviews Molecular Cell Biology *19*, 31.

620 Hill, D., and Milner, R. (1985). Insulin as a growth factor. Pediatric research *19*, 879-886.

621 Ho, C.K., Rahib, L., Liao, J.C., Sriram, G., and Dipple, K.M. (2015). Mathematical modeling of
622 the insulin signal transduction pathway for prediction of insulin sensitivity from expression
623 data. Molecular genetics and metabolism *114*, 66-72.

624 Huang, C., Wu, M., Du, J., Liu, D., and Chan, C. (2014). Systematic modeling for the insulin
625 signaling network mediated by IRS1 and IRS2. Journal of theoretical biology *355*, 40-52.

626 Humphrey, S.J., Azimifar, S.B., and Mann, M. (2015). High-throughput phosphoproteomics
627 reveals in vivo insulin signaling dynamics. Nature biotechnology *33*, 990-995.

628 Klipp, E., Liebermeister, W., Wierling, C., and Kowald, A. (2016). Systems biology: a textbook
629 (John Wiley & Sons).

630 Krishnan, N., Bonham, C.A., Rus, I.A., Shrestha, O.K., Gauss, C.M., Haque, A., Tocilj, A.,
631 Joshua-Tor, L., and Tonks, N.K. (2018). Harnessing insulin-and leptin-induced oxidation of
632 PTP1B for therapeutic development. Nature communications *9*, 1-17.

633 Krüger, M., Kratchmarova, I., Blagoev, B., Tseng, Y.-H., Kahn, C.R., and Mann, M. (2008).
634 Dissection of the insulin signaling pathway via quantitative phosphoproteomics. Proceedings
635 of the National Academy of Sciences *105*, 2451-2456.

636 Kubota, H., Noguchi, R., Toyoshima, Y., Ozaki, Y.-i., Uda, S., Watanabe, K., Ogawa, W., and
637 Kuroda, S. (2012). Temporal coding of insulin action through multiplexing of the AKT
638 pathway. Molecular cell *46*, 820-832.

639 Kubota, H., Uda, S., Matsuzaki, F., Yamauchi, Y., and Kuroda, S. (2018). In vivo decoding
640 mechanisms of the temporal patterns of blood insulin by the insulin-AKT pathway in the
641 liver. Cell systems *7*, 118-128. e113.

642 Lu, M., Wan, M., Leavens, K.F., Chu, Q., Monks, B.R., Fernandez, S., Ahima, R.S., Ueki, K.,
643 Kahn, C.R., and Birnbaum, M.J. (2012). Insulin regulates liver metabolism in vivo in the
644 absence of hepatic Akt and Foxo1. Nature medicine *18*, 388-395.

645 Maniyadath, B., Chattopadhyay, T., Verma, S., Kumari, S., Kulkarni, P., Banerjee, K., Lazarus,
646 A., Kokane, S.S., Shetty, T., and Anamika, K. (2019). Loss of hepatic oscillatory fed microRNAs
647 abrogates refed transition and causes liver dysfunctions. Cell reports *26*, 2212-2226. e2217.

648 Manning, B.D., and Toker, A. (2017). AKT/PKB signaling: navigating the network. Cell *169*,
649 381-405.

650 Mendoza, M.C., Er, E.E., and Blenis, J. (2011). The Ras-ERK and PI3K-mTOR pathways: cross-
651 talk and compensation. Trends in biochemical sciences *36*, 320-328.

652 Menge, B.A., Grüber, L., Jørgensen, S.M., Deacon, C.F., Schmidt, W.E., Veldhuis, J.D., Holst,
653 J.J., and Meier, J.J. (2011). Loss of inverse relationship between pulsatile insulin and
654 glucagon secretion in patients with type 2 diabetes. Diabetes *60*, 2160-2168.

655 Noguchi, R., Kubota, H., Yugi, K., Toyoshima, Y., Komori, Y., Soga, T., and Kuroda, S. (2013).
656 The selective control of glycolysis, gluconeogenesis and glycogenesis by temporal insulin
657 patterns. Molecular systems biology *9*, 664.

658 O'Meara, N.M., Sturis, J., Van Cauter, E., and Polonsky, K.S. (1993). Lack of control by
659 glucose of ultradian insulin secretory oscillations in impaired glucose tolerance and in non-
660 insulin-dependent diabetes mellitus. The Journal of clinical investigation *92*, 262-271.

661 O'Rahilly, S., Turner, R.C., and Matthews, D.R. (1988). Impaired pulsatile secretion of insulin
662 in relatives of patients with non-insulin-dependent diabetes. New England Journal of
663 Medicine *318*, 1225-1230.

664 Petersen, M.C., and Shulman, G.I. (2018). Mechanisms of insulin action and insulin
665 resistance. Physiological reviews *98*, 2133-2223.

666 Pørksen, N. (2002). The in vivo regulation of pulsatile insulin secretion. Diabetologia *45*, 3-
667 20.

668 Saltiel, A.R., and Kahn, C.R. (2001). Insulin signalling and the regulation of glucose and lipid
669 metabolism. Nature *414*, 799-806.

670 Sarbassov, D.D., Guertin, D.A., Ali, S.M., and Sabatini, D.M. (2005). Phosphorylation and
671 regulation of Akt/PKB by the rictor-mTOR complex. Science *307*, 1098-1101.

672 Satin, L.S., Butler, P.C., Ha, J., and Sherman, A.S. (2015). Pulsatile insulin secretion, impaired
673 glucose tolerance and type 2 diabetes. Molecular aspects of medicine *42*, 61-77.

674 Schmelzle, K., Kane, S., Gridley, S., Lienhard, G.E., and White, F.M. (2006). Temporal
675 dynamics of tyrosine phosphorylation in insulin signaling. Diabetes *55*, 2171-2179.

676 Sedaghat, A.R., Sherman, A., and Quon, M.J. (2002). A mathematical model of metabolic
677 insulin signaling pathways. American Journal of Physiology-Endocrinology and Metabolism
678 *283*, E1084-E1101.

679 Shaw, E., Talwadekar, M., Rashida, Z., Mohan, N., Acharya, A., Khatri, S., Laxman, S., and
680 Kolthur-Seetharam, U. (2020). Anabolic SIRT4 Exerts Retrograde Control over TORC1
681 Signaling by Glutamine Sparing in the Mitochondria. Molecular and Cellular Biology *40*.

682 Shaw, R.J., and Cantley, L.C. (2006). Ras, PI (3) K and mTOR signalling controls tumour cell
683 growth. Nature *441*, 424-430.

684 Shimobayashi, M., Albert, V., Woelnerhanssen, B., Frei, I.C., Weissenberger, D., Meyer-
685 Gerspach, A.C., Clement, N., Moes, S., Colombi, M., and Meier, J.A. (2018). Insulin resistance
686 causes inflammation in adipose tissue. The Journal of clinical investigation *128*, 1538-1550.

687 Shinar, G., Milo, R., Martínez, M.R., and Alon, U. (2007). Input–output robustness in simple
688 bacterial signaling systems. Proceedings of the National Academy of Sciences *104*, 19931-
689 19935.

690 Shoelson, S.E., Lee, J., and Goldfine, A.B. (2006). Inflammation and insulin resistance. The
691 Journal of clinical investigation *116*, 1793-1801.

692 Silva-Rocha, R., and de Lorenzo, V. (2010). Noise and robustness in prokaryotic regulatory
693 networks. Annual review of microbiology *64*, 257-275.

694 Somvanshi, P.R., Tomar, M., and Kareenhalli, V. (2019). computational Analysis of insulin-
695 Glucagon Signalling network: implications of Bistability to Metabolic Homeostasis and
696 Disease states. Scientific reports *9*, 1-11.

697 Sonntag, A.G., Dalle Pezze, P., Shanley, D.P., and Thedieck, K. (2012). A modelling–
698 experimental approach reveals insulin receptor substrate (IRS)-dependent regulation of
699 adenosine monosphosphate-dependent kinase (AMPK) by insulin. The FEBS journal *279*,
700 3314-3328.

701 Thattai, M., and Van Oudenaarden, A. (2001). Intrinsic noise in gene regulatory networks.
702 Proceedings of the National Academy of Sciences *98*, 8614-8619.

703 Vander Haar, E., Lee, S.-i., Bandhakavi, S., Griffin, T.J., and Kim, D.-H. (2007). Insulin
704 signalling to mTOR mediated by the Akt/PKB substrate PRAS40. Nature cell biology *9*, 316-
705 323.

706 Vigneri, R., Sciacca, L., and Vigneri, P. (2020). Rethinking the Relationship between Insulin
707 and Cancer. Trends in Endocrinology & Metabolism.

708 Vinayagam, A., Kulkarni, M.M., Sopko, R., Sun, X., Hu, Y., Nand, A., Villalta, C., Moghimi, A.,
709 Yang, X., and Mohr, S.E. (2016). An integrative analysis of the InR/PI3K/Akt network
710 identifies the dynamic response to insulin signaling. Cell reports *16*, 3062-3074.

711 Vinod, P.K.U., and Venkatesh, K.V. (2009). Quantification of the effect of amino acids on an
712 integrated mTOR and insulin signaling pathway. Molecular BioSystems *5*, 1163-1173.

713 Wilson, M.Z., Ravindran, P.T., Lim, W.A., and Toettcher, J.E. (2017). Tracing information flow
714 from Erk to target gene induction reveals mechanisms of dynamic and combinatorial
715 control. Molecular cell *67*, 757-769. e755.

716 Yugi, K., Kubota, H., Toyoshima, Y., Noguchi, R., Kawata, K., Komori, Y., Uda, S., Kunida, K.,
717 Tomizawa, Y., and Funato, Y. (2014). Reconstruction of insulin signal flow from
718 phosphoproteome and metabolome data. Cell reports *8*, 1171-1183.

719 Zhao, G., Wirth, D., Schmitz, I., and Meyer-Hermann, M. (2017). A mathematical model of
720 the impact of insulin secretion dynamics on selective hepatic insulin resistance. Nature
721 communications *8*, 1-10.

722

Figure Legends

Figure 1: **Iterative experimental-mathematical approach reveals distinct insulin signaling kinetics**

(A) Schematic of the insulin/IGF signaling pathway. Components involved in metabolic and mitogenic arms are shown in blue and green, respectively. Phosphorylations measured in this study are highlighted in red. (B) Experimental paradigm and workflow for assaying signaling in response to one step stimulation. (C) Representative blots for levels of $pAKT^{T308}$ and $pAKT^{S473}$ following insulin stimulation, as indicated. Total AKT and actin were used for normalization. See more in Figure 1- figure supplement 1E-F and 2A-B. (D) and (E) Quantitation for temporal changes in $pAKT^{S473}$ (D) and $pAKT^{T308}$ (E) from experimental data shown in C. Fold changes for each concentration are with respective to their own 0m time point. Data presented is mean ± s.e.m. (N=4, n=4). (F) and (G) Quantitation for temporal changes in $pAKT^{S473}$ (F) and $pAKT^{T308}$ (G) from mathematical simulations using differential equations. (H) Kinetic behavior of phosphorylated $pAKT^{T308}$ and $pAKT^{S473}$ molecules at 1 nM insulin from stochastic simulations. The band represents standard deviation. (I) z-score giving degree of concordance between simulated and experimental data.

Figure 2: **Continuous variable parameters and high/low pass filters determine concentration dependent insulin response**

(A) Extent of change in phosphorylation at $pAKT^{T308}$ and $pAKT^{S473}$ across time points between 0.1 and 1 nM insulin. (B) Phase diagram depicting relationship between peak intensity and decay time from simulated data. (C) Estimated peak amplitude for

745 signaling components as a function of varying insulin concentrations depicts dynamic range.
746 (D) Dynamic range for signaling components computed from (C), as labeled.

747 **Figure 3: Kinetic gates and maximum connectedness is associated with robust topology**
748 **under normo-insulinemic states**

749 (A) K_{ON}/K_{OFF} ratios for phosphorylations across the signaling cascade. Insulin concentrations
750 of 0.1-10 nM are depicted separately. Numbers on the x-axis represent phosphorylation
751 events as detailed in Figure 3 – figure supplement 1A. Yellow band refers to the kinetic
752 barrier applied between 0.1-10, representing a 10-fold change. (B) Noise in signal for
753 phosphorylation at $pAKT^{T308}$ and $pAKT^{S473}$ in response to different insulin concentrations, as
754 indicated. (C) Correlation matrix depicts degree of relatedness between phosphorylation
755 events and their evolution with increasing insulin concentration. (D) Network analysis
756 depicting degree of connectedness across insulin concentrations, as indicated. Dashed line
757 represents negative correlation. Significance in correlation: White ($p<0.05$) <Blue ($p<0.005$)
758 <Green ($p<0.0005$) <Yellow ($p<0.00001$) as observed by Student's t-test. (E) Number of
759 edges and nodes in a 1 nM network substituted with 10 nM values, as indicated. (F)
760 Network maps of 1 nM insulin perturbed with 10 nM $pAKT^{T308}$ (a) and $pAKT^{S473}$ (b)

761 **Figure 4: Pulsatile fasting insulin rewires response to fed insulin inputs akin to memory**

762 (A) Experimental paradigm for mimicking fasted and fed insulin stimulation. P1-P4 indicate
763 0.1 nM insulin pulses. (B-D) Quantitation for temporal changes in phosphorylations at
764 $pAKT^{T308}$ (B), $pAKT^{S473}$ (C) and $pERK^{T202/Y204}$ (D) following insulin treatment as in A. Fold
765 changes for each concentration are with respective to their own 0m time point. Data
766 presented is mean ± s.e.m. (N=4). (E) Network analysis showing connectivity among
767 signaling components after treatment with 1 nM insulin following fasted insulin inputs, as in
768 A. Dashed line represents negative correlation. Significance in correlation: White ($p<0.05$)

769 <Blue ($p<0.005$) <Green ($p<0.0005$) <Yellow ($p<0.00001$) as observed by Student's t-test. (F)
770 Heat maps for changes in gene expression downstream to insulin signaling in response to
771 constant 0.1 nM and 1 nM, and 1 nM insulin following fasted insulin inputs (1 nM adapted,
772 as in A) (N=2, n=3)

773 **Figure 5**: **Repeated stimulation by fed insulin abrogates the synergy between the**
774 **metabolic and mitogenic arms of signaling**

775 (A) Experimental paradigm for repeated stimulation with 1nM insulin. (B-D) Quantitation for
776 temporal changes in phosphorylations at $pAKT^{T308}$ (B), $pAKT^{S473}$ (C) and $pERK^{T202/Y204}$ (D)
777 following repeated insulin stimulation. Fold changes for each concentration are with
778 respective to their own 0m time point. Data presented is mean ± s.e.m. (N=4). (E) Network
779 analysis showing connectivity among signaling components after repeated insulin
780 stimulation, as in A. Dashed line represents negative correlation. Significance in correlation:
781 White ($p<0.05$) <Blue ($p<0.005$) <Green ($p<0.0005$) <Yellow ($p<0.00001$) as observed by
782 Student's t-test. (F) Heat maps for changes in gene expression downstream to insulin
783 signaling in response to repeated insulin stimulation (N=2, n=3)

784 **Figure 1 – figure supplement 1**:

785 (A-B) Normalization controls to correct for baseline signal. Representative samples were
786 loaded to ensure that zero-minute time points across experiments were similar. (B) was
787 over-exposed to get signal at zero minute. (C) Control for experimental paradigm to score
788 for insulin inputs. Treatment with only high/low glucose and amino acid containing culture
789 medium does not activate AKT signaling and indicates that the changes in phosphorylation
790 are insulin dependent. (D) Quantitation for temporal changes in phosphorylations for C. (E
791 and F) Representative blots for levels of $pERK^{T202/Y204}$, $pS6K^{T389}$ and $pGSK3\beta^{S9}$ following

792 insulin stimulation of 0.1 and 1 nM, as indicated. Respective total proteins and actin were
793 used for normalization

794 **Figure 1 – figure supplement 2**

795 (A and B) Representative blots for levels of pERK$^{T202/Y204}$, pS6K^{T389} and pGSK3β^{S9} following
796 insulin stimulation of 10 and 100 nM, as indicated. Respective total proteins and actin were
797 used for normalization. (C) Comparison of area under the curve (AUC) with increasing insulin
798 concentration. Asterisk depicts p values (*p<0.05, **p<0.005 and ***p<0.0005) as observed
799 by Student's t-test. (D) True discovery rates computed across insulin concentrations, see
800 methods.

801 **Figure 1 – figure supplement 3**

802 (A-C) Quantitation for temporal changes in pGSK3β^{S9}(A), pS6K^{T389} (B) and pERK$^{T202/Y204}$ (C)
803 from experimental data shown in Figure 1 – figure supplement 1E-F and 2A-B. Fold changes
804 for each concentration are with respective to their own 0m time point. Data presented is
805 mean ± s.e.m. (N=4, n=4). (D-F) Quantitation for temporal changes in pGSK3β^{S9} (D),
806 pS6K^{T389} (E) and pERK$^{T202/Y204}$ (F) from mathematical simulations using differential equations.
807 (G) Simulated temporal changes in pIR, pmTORC1 and pmTORC2 following insulin
808 stimulation, as indicated. (H) False discovery rates giving degree of concordance between
809 simulated and experimental data, see methods

810 **Figure 2 – figure supplement 1**

811 (A) Representative blots for level of pAKT^{S473} kinetics under insulin concentrations of 0.3 and
812 0.6 nM. Total AKT and actin were used for normalization. (B) Concordance between
813 experimental and simulated data for extent of phosphorylation at pAKT^{S473} following
814 stimulation by intermediate insulin concentrations. (C) Estimated final amplitude for
815 signaling components at 120m as a function of varying insulin concentrations

Figure 3 – figure supplement 1

(A) Reactions corresponding to numbers on y-axis in Figure 3A. (B) Ordinary differential equations corresponding to reactions mentioned in A. (C) Pearson r and corresponding p values used for computing networks in Figure 3D. and Figure 3- figure supplement 2

Figure 3 – figure supplement 2

Pearson r and corresponding p values used for computing networks in Figure 3F and Figure 3- figure supplement 3

Figure 3 – figure supplement 3

(A) Network maps of 1 nM insulin perturbed with 10 nM $pAKT^{T308\ and\ S473}$ (a), $pERK^{T202/Y204}$ (b), $pGSK3b^{S9}$ (c) and $pS6K^{T389}$ (d). (B) Number of edges and nodes in a 0.1 nM network substituted with 10 nM values, as indicated. (C) Network maps of 0.1 nM insulin perturbed with 10 nM $pAKT^{T308}$ (a) and $pAKT^{S473}$ (b). (D) Network maps of 0.1 nM insulin perturbed with 10 nM $pAKT^{T308\ and\ S473}$ (a), $pERK^{T202/Y204}$ (b), $pGSK3b^{S9}$ (c) and $pS6K^{T389}$ (d).

Figure 4 – figure supplement 1

(A-D) Representative blots for levels of $pAKT^{T308}$ (A), $pAKT^{S473}$ (A), $pERK^{T202/Y204}$ (B), $pS6K^{T389}$ (C) and $pGSK3\beta^{S9}$ (D) following pulsatile insulin stimulation, as indicated in Figure 4A. Respective total proteins and actin were used for normalization kinetics. (E and F) Quantitation for temporal changes in phosphorylations at $pGSK3\beta^{S9}$ (E) and $pS6K^{T389}$ (F) following insulin pulses. Fold changes for each concentration are with respective to their own 0m time point. Data presented is mean ± s.e.m. (N=4)

Figure 5 – figure supplement 1

(A-D) Representative blots for levels of $pAKT^{T308}$ (A), $pAKT^{S473}$ (A), $pERK^{T202/Y204}$ (B), $pS6K^{T389}$ (C) and $pGSK3\beta^{S9}$ (D) following repeated insulin stimulation, as indicated in Figure 5A. Respective total proteins and actin were used for normalization kinetics. (E and F)

840 Quantitation for temporal changes in phosphorylations at pGSK3β^{S9} (E) and pS6K^{T389} (F)
841 following repeated insulin stimulation. Fold changes for each concentration are with
842 respective to their own 0m time point. Data presented is mean ± s.e.m. (N=4).

Source Data

Figure 1 – source data 1: Blot intensity and quantitation for $pAKT^{S473}$ and $pAKT^{T308}$

Figure 1 – source data 2: Values for $pAKT^{S473}$ and $pAKT^{T308}$ from deterministic simulations used for plotting Figure 1F-G

Figure 1 – source data 3: Values for $pAKT^{S473}$ from stochastic simulations used for plotting Figure 1H

Figure 1 – source data 4: z-score computation for concordance between simulated and experimental data

Figure 1 – figure supplement 1 – source data 1: Blot intensity and quantitation for Figure 1 - figure supplement 1C-D

Figure 1 – figure supplement 2 – source data 1: Calculations for computing area under the curve

Figure 1 – figure supplement 2 – source data 2: TDR computation for comparison across insulin concentration

Figure 1 – figure supplement 3 – source data 1: Blot intensity and quantitation for $pGSK3\beta^{S9}$, $pS6K^{T389}$ and $pERK^{T202/Y204}$ used for plotting Figure 1 – figure supplement 3A-C

Figure 1 – figure supplement 3 – source data 2: Values for $pGSK3\beta^{S9}$, $pS6K^{T389}$ and $pERK^{T202/Y204}$ from deterministic simulations used for plotting Figure 1 – figure supplement 3D-F

Figure 1 – figure supplement 3 – source data 3: Values for pIR, pmTORC1 and pmTORC2 from deterministic simulations used for plotting Figure 1 – figure supplement 3G

Figure 1 – figure supplement 3 – source data 4: FDR calculations for degree of concordance between simulated and experimental data

Figure 2 – source data 1: Percentage gain computation w.r.t. Figure 2A

867 **Figure 2 – source data 2:** Values for peak intensity and decay time used for plotting Figure
868 2B

869 **Figure 2 – source data 3:** Values for peak intensity used to plot Figure 2C

870 **Figure 2 – source data 4:** Computation of dynamic range for Figure 2D

871 **Figure 2 – figure supplement 1 – source data 1:** Blot intensity and quantitation for extent of
872 phosphorylation at $pAKT^{S473}$ following stimulation by intermediate insulin concentrations in
873 Figure 2- figure supplement 1A-B

874 **Figure 2 – figure supplement 1 – source data 2:** Values for final intensity at 120min. used to
875 plot Figure 2- figure supplement 1C

876 **Figure 3 – source data 1:** K_{ON}/K_{OFF} used for plotting Figure 3A

877 **Figure 3 – source data 2:** Coefficient of variation used for plotting Figure 3B

878 **Figure 3 – source data 3:** Computations for Pearson r and statistical significance used to
879 construct Figure 3C

880 **Figure 3 – source data 4:** Values for edges and nodes corresponding to Figure 3E and
881 Figure3- figure supplement 3B

882 **Figure 3 – figure supplement 1 – source data 1:** Rate constants corresponding to equations
883 in Figure 3- figure supplement

884 **Figure 4 – source data 1:** Blot intensity and quantitation for extent of phosphorylation at
885 $pAKT^{S473}$, $pAKT^{T308}$ and $pERK^{T202/Y204}$ corresponding to Figure 4B-D

886 **Figure 4 – source data 2:** Computations for Pearson r and statistical significance used to
887 construct Figure 4E

888

889 **Figure 4 – source data 3:** Ct values for changes in gene expression corresponding to Figure
890 4F

Figure 4 – figure supplement 1 – source data 1: Blot intensity and quantitation for extent of phosphorylation at pGSK3β^{S9} and pS6K^{T389} corresponding to Figure 4- figure supplement 1E-F

Figure 5 – source data 1: Blot intensity and quantitation for extent of phosphorylation at pAKT^{S473}, pAKT^{T308} and pERK$^{T202/Y204}$ corresponding to Figure 5B-D

Figure 5 – source data 2: Computations for Pearson r and statistical significance used to construct Figure 5E

Figure 5 – source data 3: Ct values for changes in gene expression corresponding to Figure 5F

Figure 5 – figure supplement 1 – source data 1: Blot intensity and quantitation for extent of phosphorylation at pGSK3β^{S9} and pS6K^{T389} corresponding to Figure 5- figure supplement 1B-C

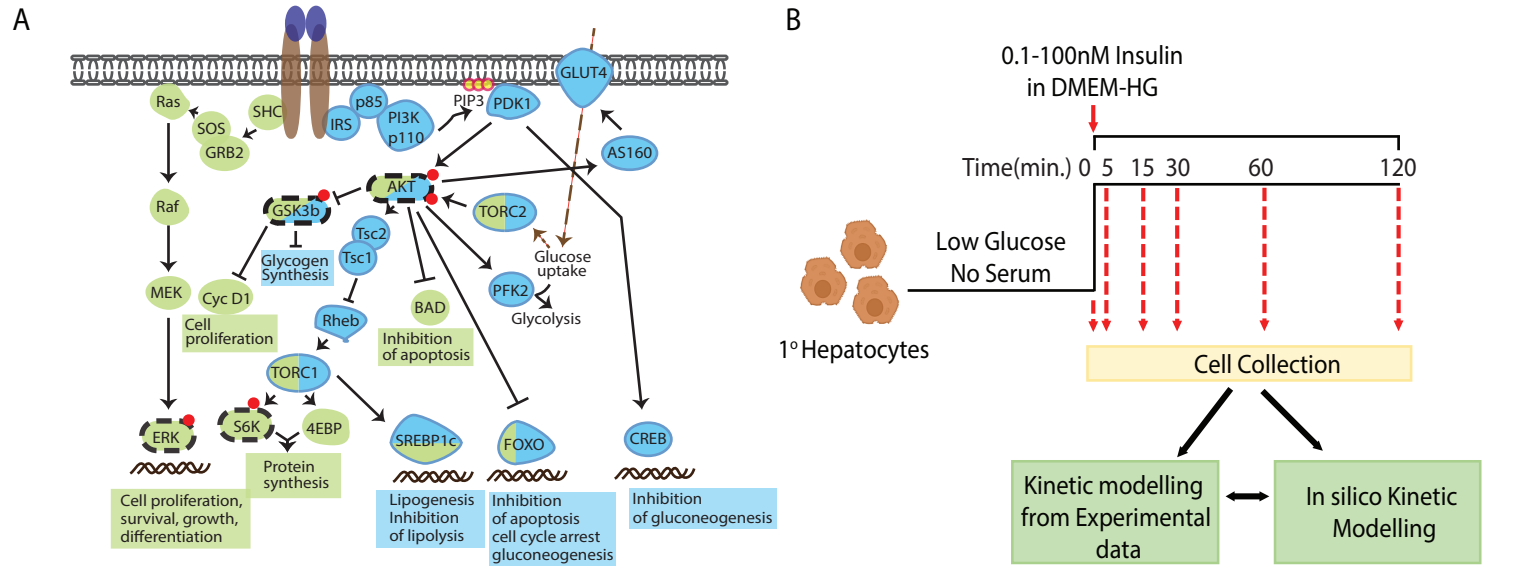

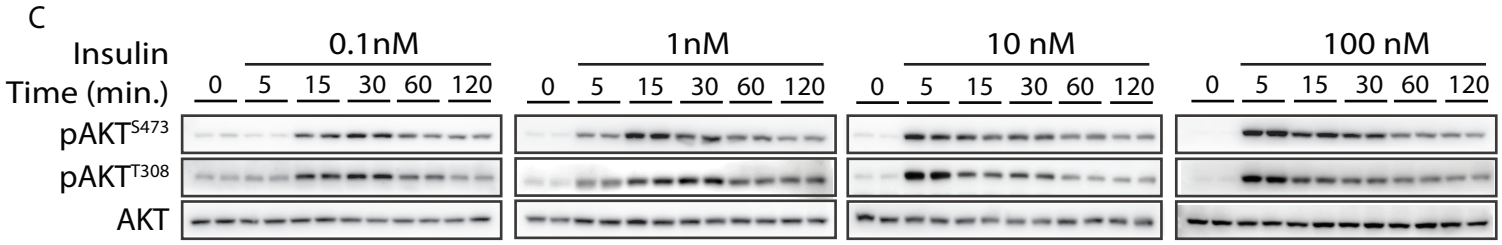

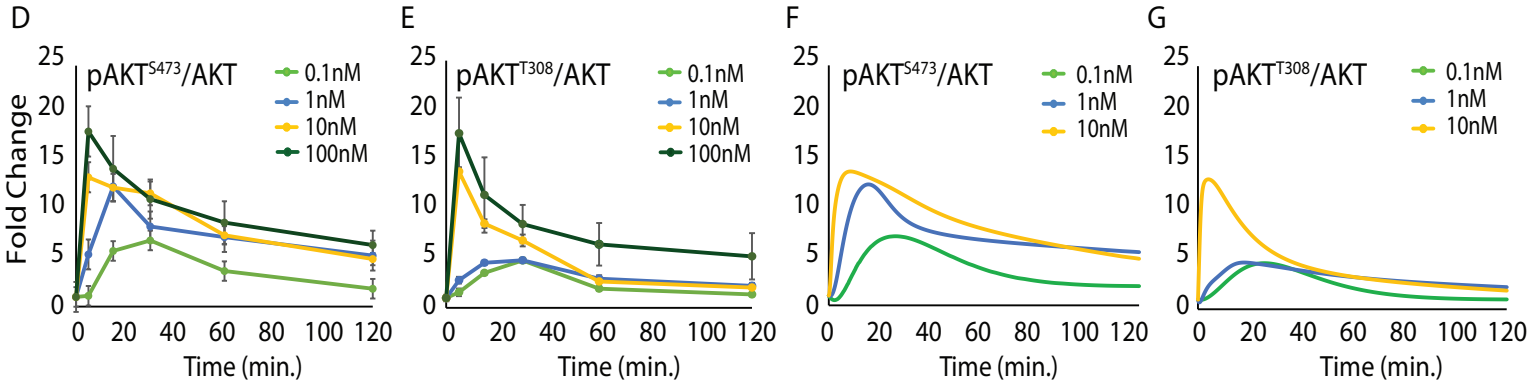

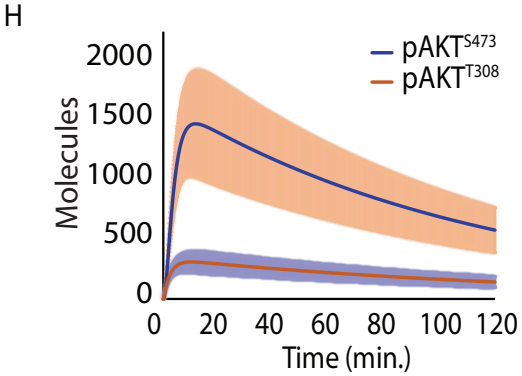

I

z-score	0.1 nM	1 nM	10 nM
pAKT^{S473}	0.7953	0.0029	-0.1157
pAKT^{T308}	-0.4336	0.0460	0.0411
pS6K^{T389}	-1.1231	1.3741	0.6385
pGSK3β^{S9}	0.3341	-0.0978	0.0814
pERK$^{T202/Y204}$	0.0236	0.3766	-0.2025

Figure 1

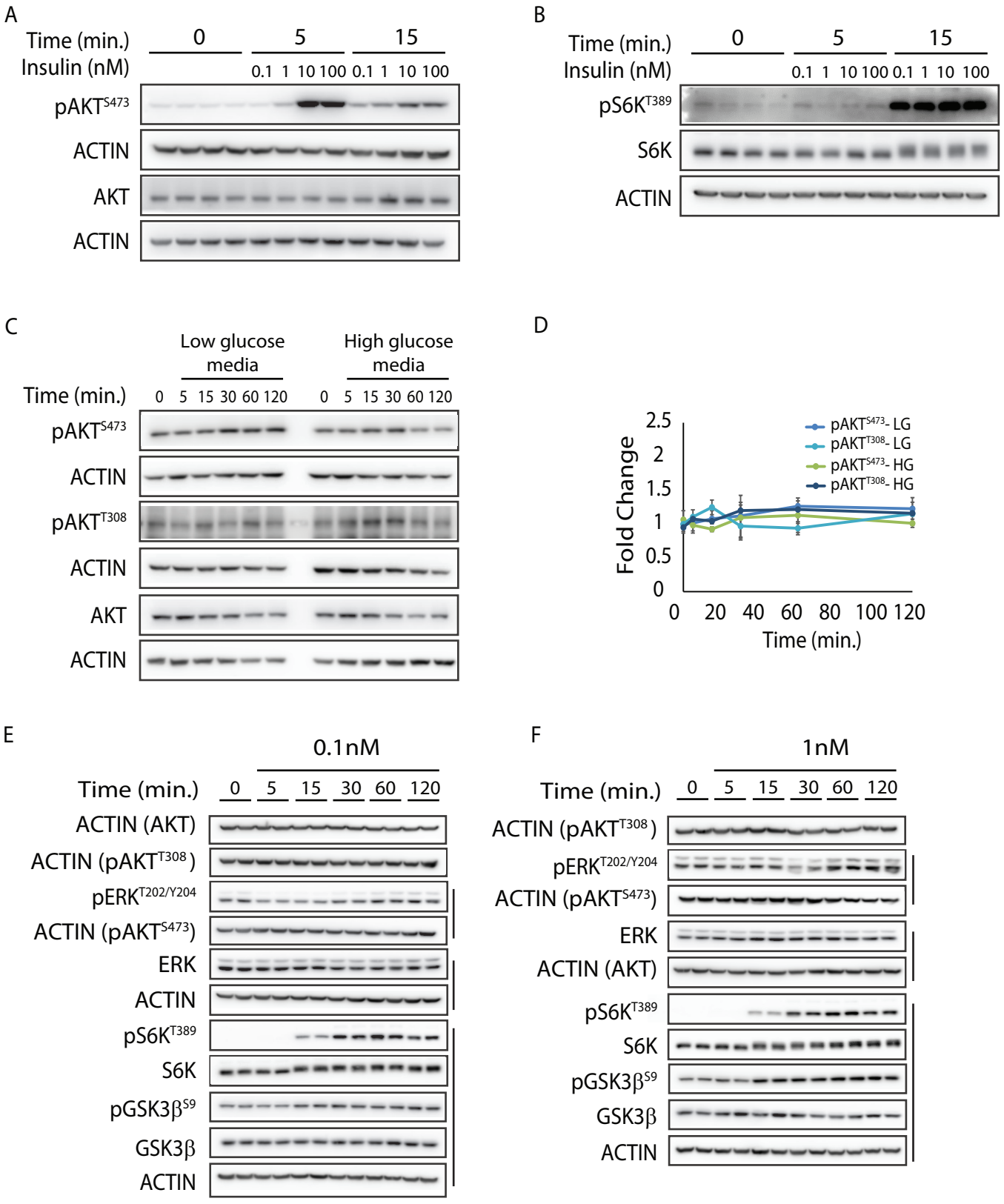

Figure 1 - figure supplement 1

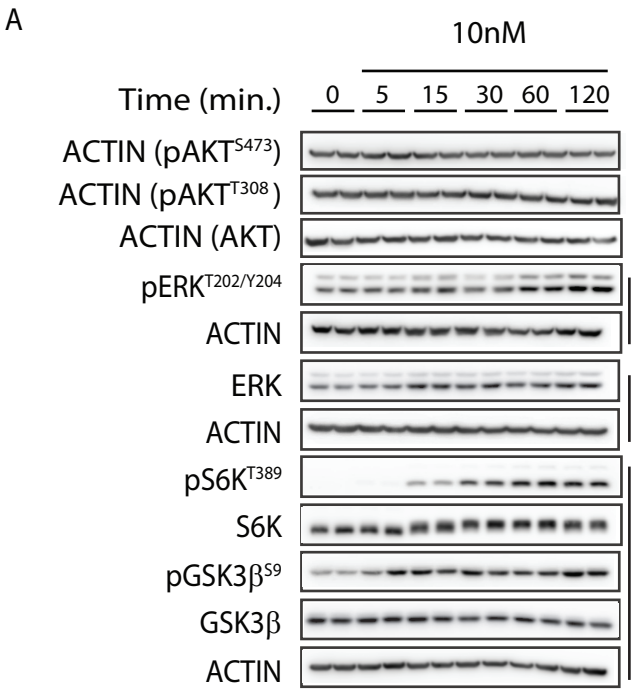

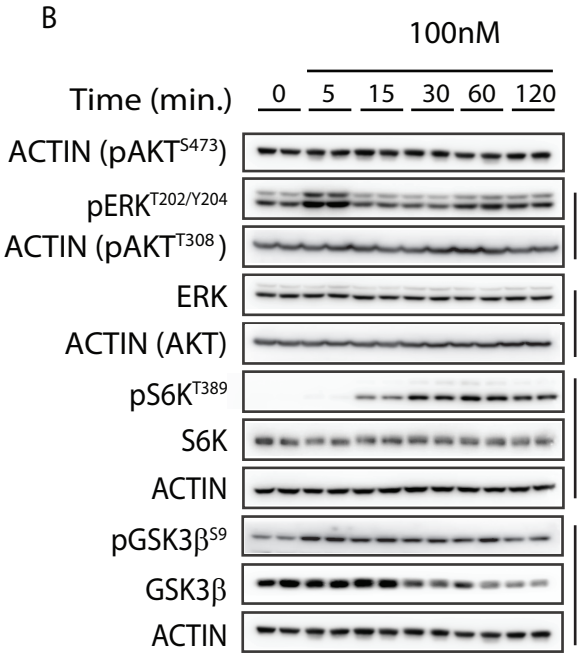

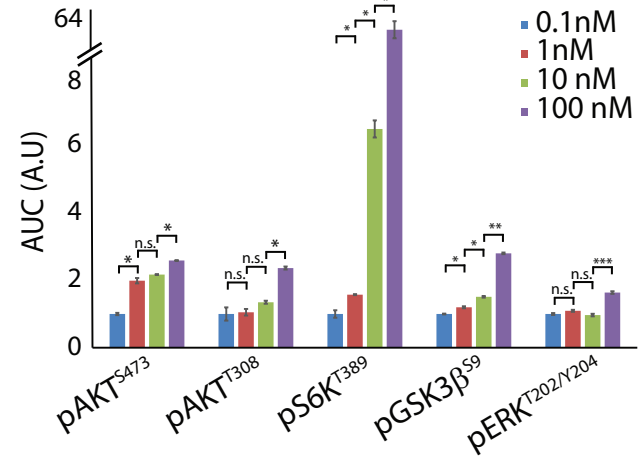

D

TDR	0.1nM vs. 1nM	0.1nM vs. 10nM	0.1nM vs. 100nM	1nM vs. 10nM	1nM vs. 100nM	10nM vs. 100nM
pAKT^{S473}	0.8	1	1	0.4	0.2	0
pAKT^{T308}	0.8	1	0.6	0.6	0.2	0
pS6K^{T389}	1	1	1	1	1	0.2
pGSK3β^{S9}	0.8	1	1	0.4	0.2	0.2
pERK$^{T202/Y204}$	0.8	1	1	0.4	0.2	0.2

Figure 1 - figure supplement 2

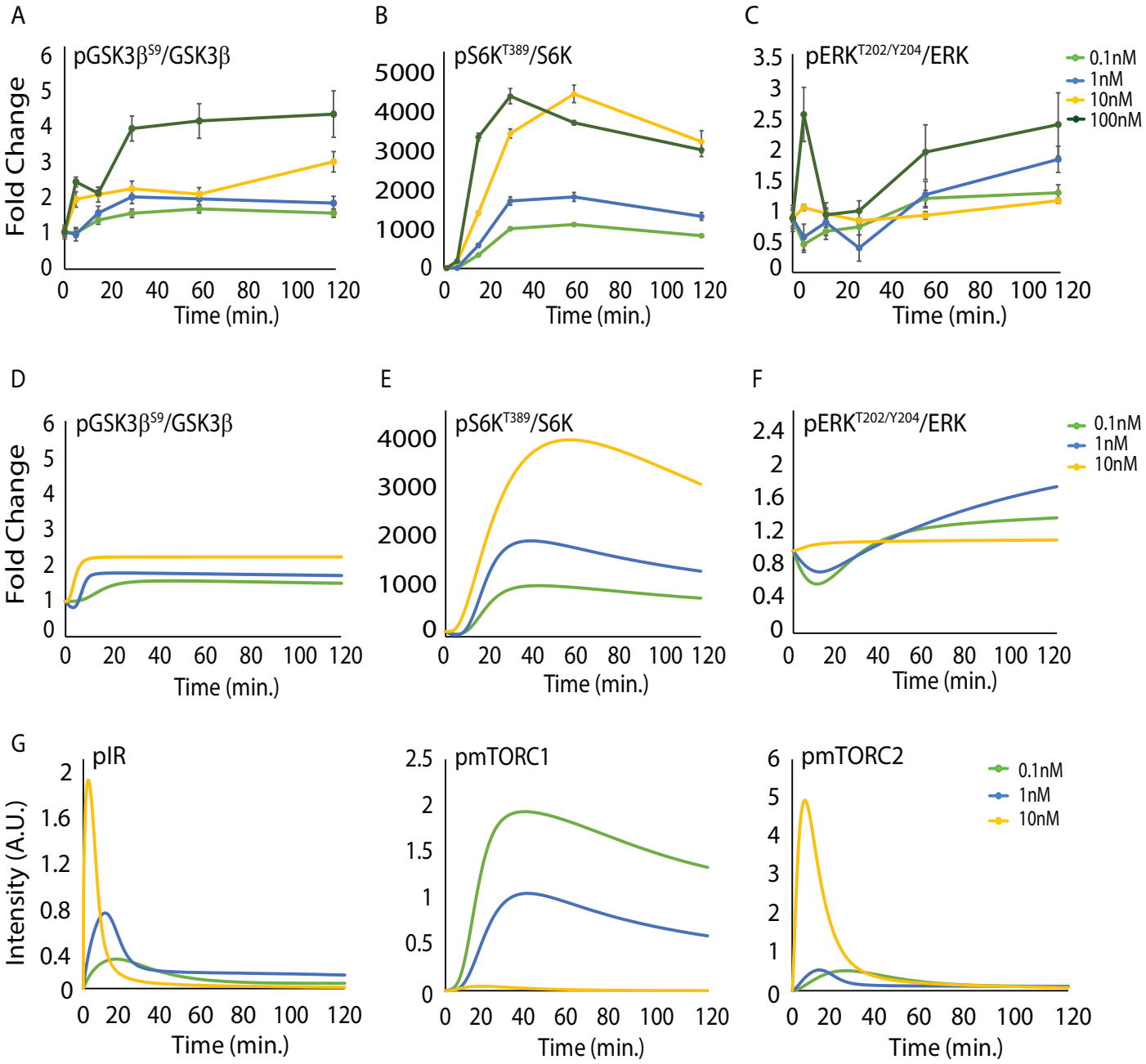

H

FDR	0.1 nM	1 nM	10 nM
pAKT^{S473}	0.167	0	0
pAKT^{T308}	0	0	0.333
pS6K^{T389}	0	0	0
pGSK3β^{S9}	0	0.167	0
pERK$^{T202/Y204}$	0	0.167	0.167

Figure 1 - figure supplement 3

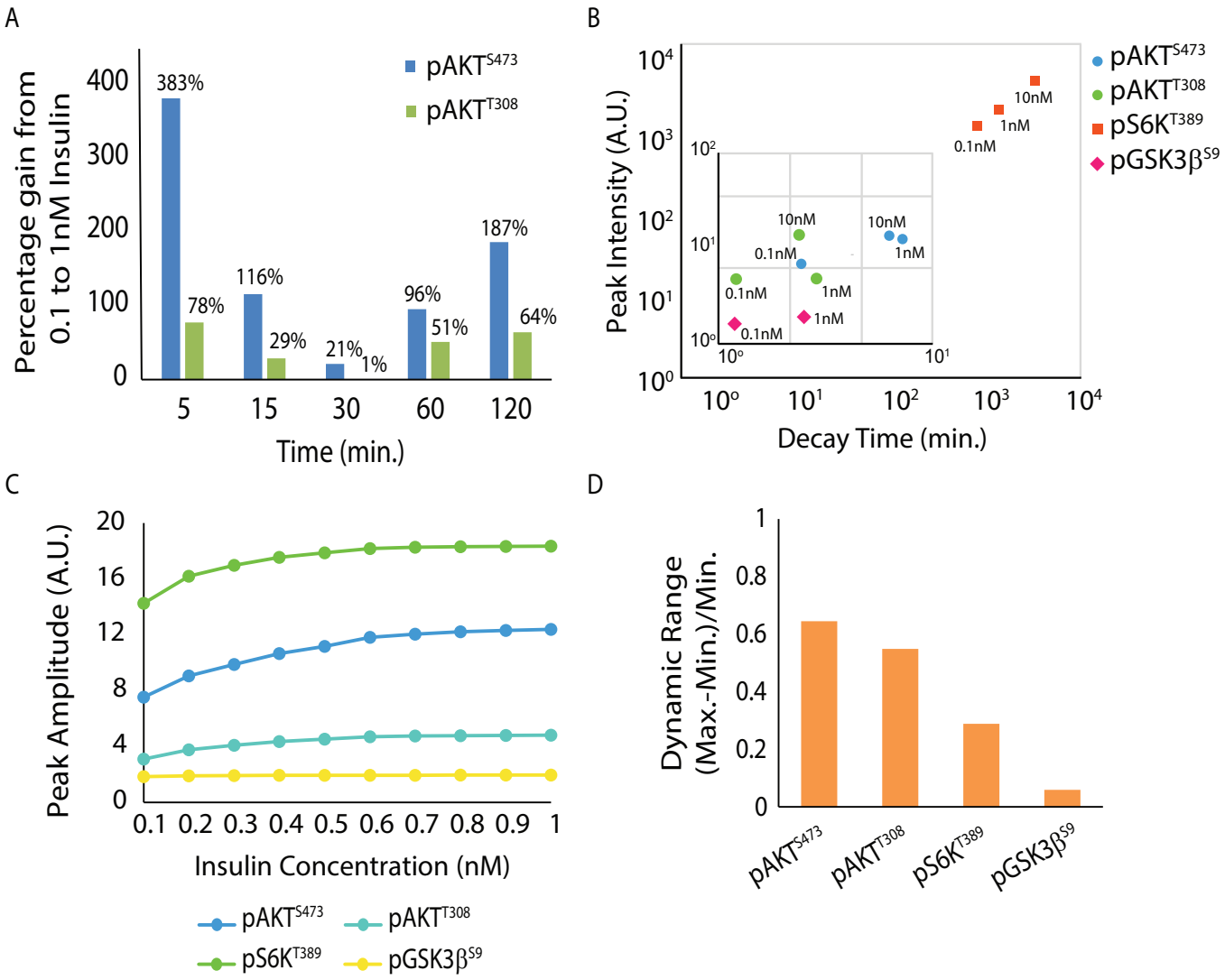
A
Percentage gain from 0.1 to 1nM Insulin
400
300
200
100
0
383%
78%
116%
29%
21%
1%
96%
51%
187%
64%
5
15
30
60
120
Time (min.)
pAKTS473
pAKTT308
B
Peak Intensity (A.U.)
Decay Time (min.)
10nM
1nM
0.1nM
pAKTS473
pAKTT308
pS6KT389
pGSK3βS9
C
Peak Amplitude (A.U.)
20
16
12
8
4
0
0.1 0.2 0.3 0.4 0.5 0.6 0.7 0.8 0.9 1
Insulin Concentration (nM)
pAKTS473
pAKTT308
pS6KT389
pGSK3βS9
D
Dynamic Range (Max.-Min.)/Min.
1
0.8
0.6
0.4
0.2
0
pAKTS473
pAKTT308
pS6KT389
pGSK3βS9

Figure 2

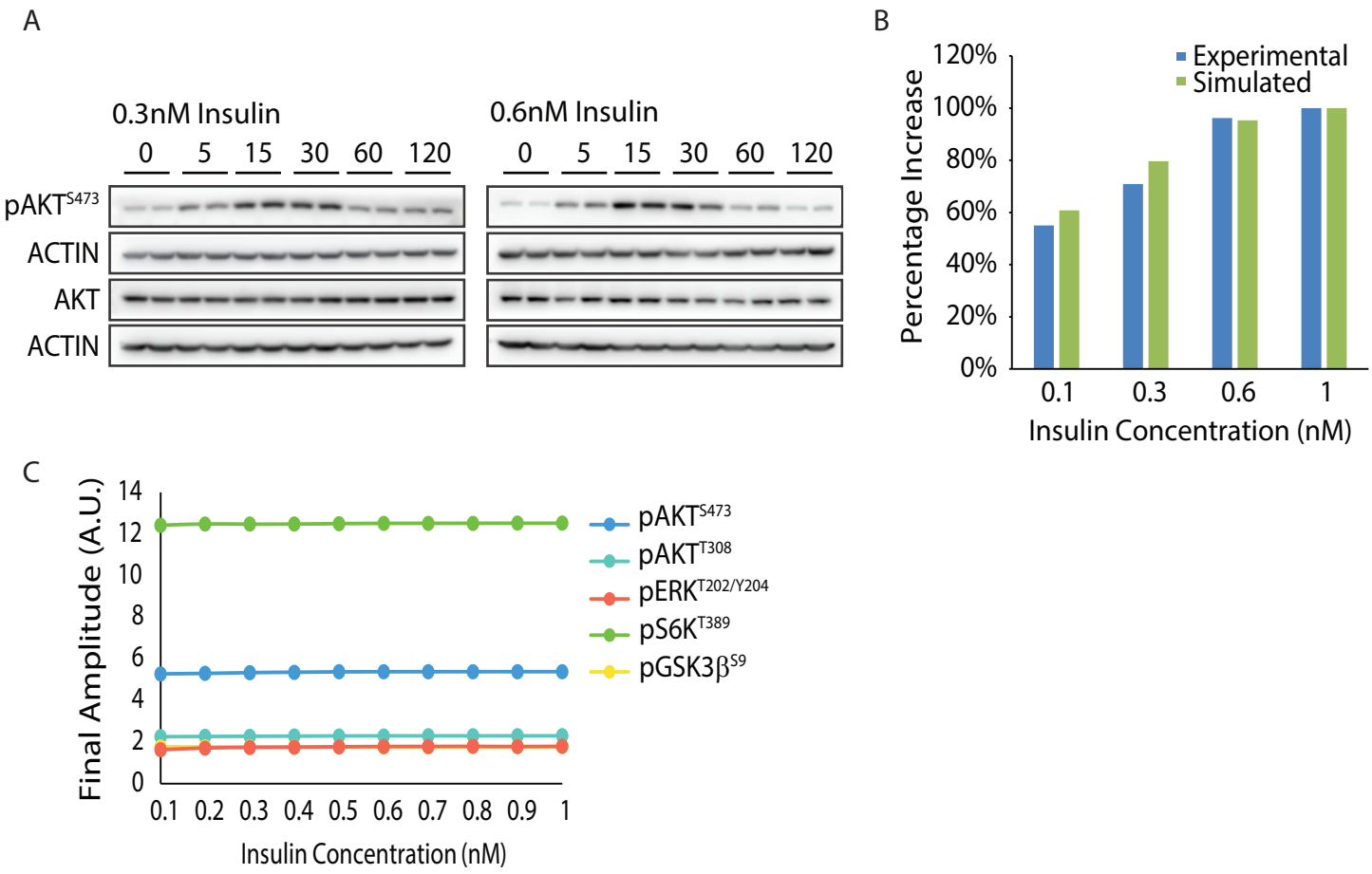

Figure 2 - figure supplement 1

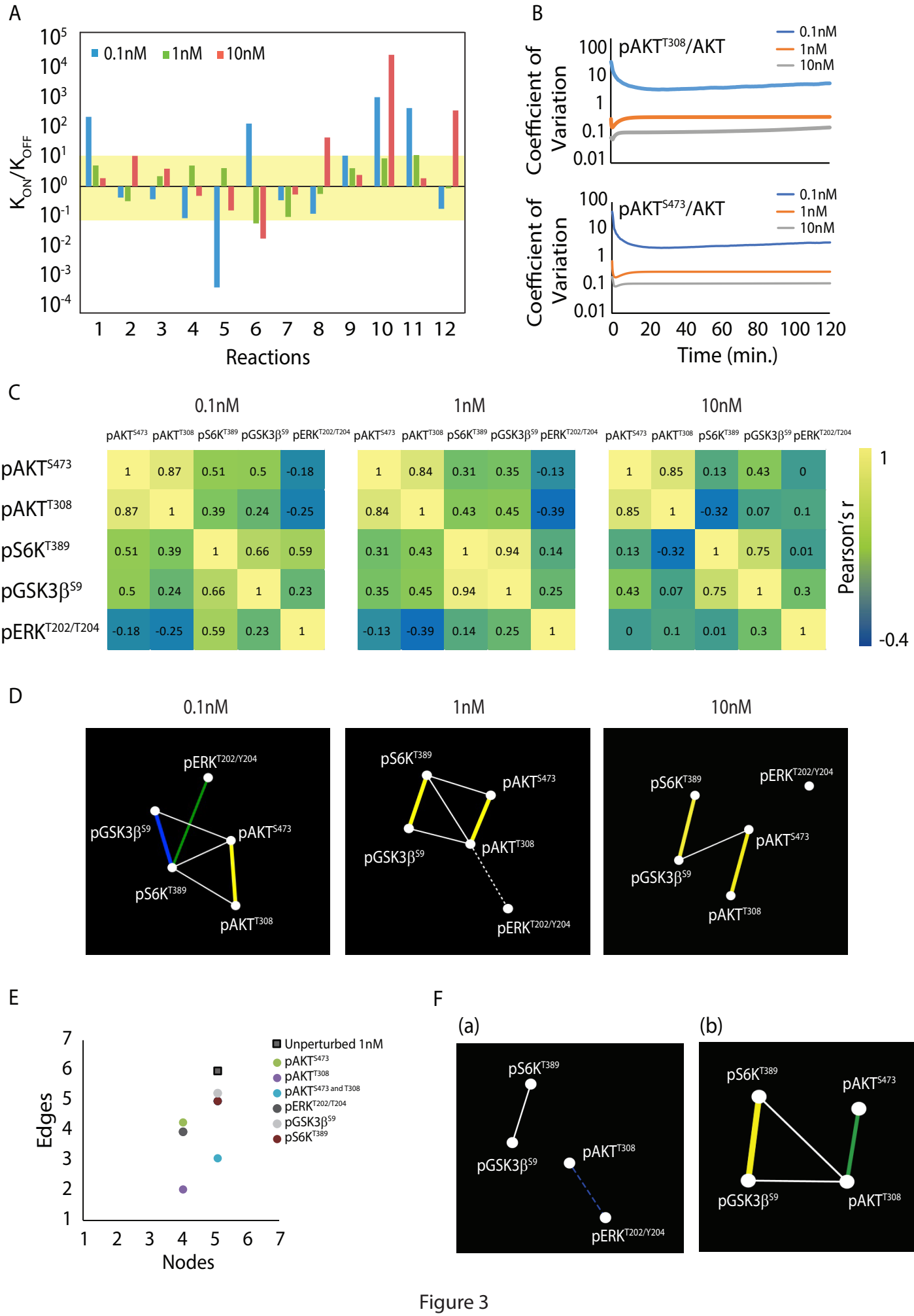
A
0.1nM
1nM
10nM
K_{ON}/K_{OFF}
Reactions
B
pAKT^{T308}/AKT
pAKT^{S473}/AKT
Coefficient of Variation
Time (min.)
C
0.1nM
1nM
10nM
pAKT^{S473}
pAKT^{T308}
pS6K^{T389}
pGSK3β^{S9}
pERK$^{T202/T204}$
Pearson's r
D
pERK$^{T202/Y204}$
pGSK3β^{S9}
pAKT^{S473}
pS6K^{T389}
pAKT^{T308}
E
Edges
Nodes
Unperturbed 1nM
pAKT^{S473}
pAKT^{T308}
pAKT^{S473} and T308
pERK$^{T202/T204}$
pGSK3β^{S9}
pS6K^{T389}
F
(a)
(b)

Figure 3

A

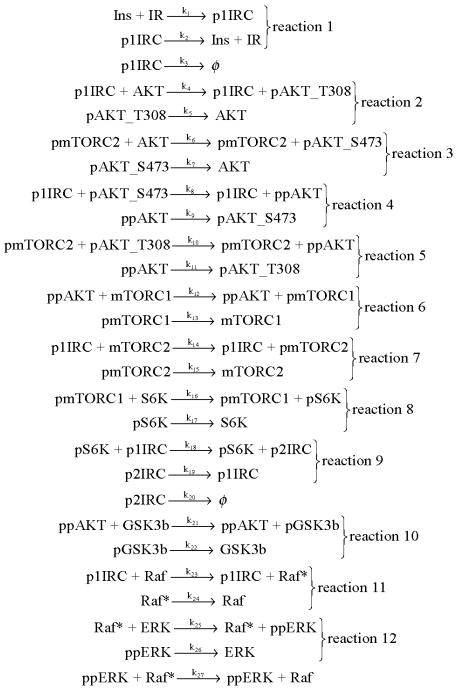

B

$$\frac{d[IR]}{dt} = -[IR].[Ins].k_1 + [p1IRC].k_2$$

$$\frac{d[p1IRC]}{dt} = [IR].[Ins].k_1 - [p1IRC].k_2 - [p1IRC].k_3 - [pS6K].[p1IRC].k_{18} + [p2IRC].k_{19}$$

$$\frac{d[pAKT\_T308]}{dt} = [p1IRC].([iAKT] - [pAKT\_T308] - [pAKT\_S473] - [ppAKT]).k_4 - [pAKT\_T308].k_5 - [pmTORC2].[pAKT\_T308].k_{10} + [ppAKT].k_{11}$$

$$\frac{d[pAKT\_S473]}{dt} = [pmTORC2].([iAKT] - [pAKT\_T308] - [pAKT\_S473] - [ppAKT]).k_6 - [pAKT\_S473].k_7 - [p1IRC].[pAKT\_S473].k_8 + [ppAKT].k_9$$

$$\frac{d[ppAKT]}{dt} = [p1IRC].[pAKT\_S473].k_8 - [ppAKT].k_9 + [pmTORC2].[pAKT\_T308].k_{10} - [ppAKT].k_{11}$$

$$\frac{d[pmTORC1]}{dt} = [ppAKT].([imTORC1] - [pmTORC1]).k_{12} - [pmTORC1].k_{13}$$

$$\frac{d[pmTORC2]}{dt} = [p1IRC].([imTORC2] - [pmTORC2]).k_{14} - [pmTORC2].k_{15}$$

$$\frac{d[pS6K]}{dt} = [pmTORC1].([iS6K] - [pS6K]).k_{16} - [pS6K].k_{17}$$

$$\frac{d[p2IRC]}{dt} = [pS6K].[p1IRC].k_{18} - [p2IRC].k_{19} - [p2IRC].k_{20}$$

$$\frac{d[pGSK3b]}{dt} = [ppAKT].([iGSK3b] - [pGSK3b]).k_{21} - [pGSK3b].k_{22}$$

$$\frac{d[Raf*]}{dt} = [p1IRC].([iRaf] - [Raf*]).k_{23} - [Raf*].k_{24} - [ppERK].[Raf*].k_{27}$$

$$\frac{d[ppERK]}{dt} = [Raf*].([iERK] - [ppERK]).k_{25} - [ppERK].k_{26}$$

C

0.1nM						1nM						10nM				
Source	Target	Interaction	Pearson r	p value		Source	Target	Interaction	Pearson r	p value		Source	Target	Interaction	Pearson r	p value
$pAKT^{S473}$	$pAKT^{T308}$	pc	0.8732	0.0001		$pAKT^{S473}$	$pAKT^{T308}$	pc	0.8408	0.0001		$pAKT^{S473}$	$pAKT^{T308}$	pc	0.8451	0.0001
$pAKT^{S473}$	$pS6K^{T389}$	pc	0.5068	0.0115		$pAKT^{S473}$	$pS6K^{T389}$	pc	0.3085	0.1425		$pAKT^{S473}$	$pS6K^{T389}$	pc	0.1315	0.5403
$pAKT^{S473}$	$pGSK3b^{S9}$	pc	0.4997	0.0129		$pAKT^{S473}$	$pGSK3b^{S9}$	pc	0.3549	0.0888		$pAKT^{S473}$	$pGSK3b^{S9}$	pc	0.4332	0.0345
$pAKT^{S473}$	$pERK^{T202/Y204}$	pc	-0.1768	0.4086		$pAKT^{S473}$	$pERK^{T202/Y204}$	pc	-0.125	0.5607		$pAKT^{S473}$	$pERK^{T202/Y204}$	pc	0.001001	0.9963
$pAKT^{T308}$	$pS6K^{T389}$	pc	0.3899	0.0596		$pAKT^{T308}$	$pS6K^{T389}$	pc	0.4316	0.0352		$pAKT^{T308}$	$pS6K^{T389}$	pc	-0.3187	0.1291
$pAKT^{T308}$	$pGSK3b^{S9}$	pc	0.2441	0.2503		$pAKT^{T308}$	$pGSK3b^{S9}$	pc	0.4546	0.0256		$pAKT^{T308}$	$pGSK3b^{S9}$	pc	0.0665	0.7575
$pAKT^{T308}$	$pERK^{T202/Y204}$	pc	-0.2486	0.2415		$pAKT^{T308}$	$pERK^{T202/Y204}$	pc	-0.3916	0.0584		$pAKT^{T308}$	$pERK^{T202/Y204}$	pc	0.1014	0.6375
$pS6K^{T389}$	$pGSK3b^{S9}$	pc	0.6607	0.0004		$pS6K^{T389}$	$pGSK3b^{S9}$	pc	0.9363	0.0001		$pS6K^{T389}$	$pGSK3b^{S9}$	pc	0.747	<0.0001
$pS6K^{T389}$	$pERK^{T202/Y204}$	pc	0.588	0.0025		$pS6K^{T389}$	$pERK^{T202/Y204}$	pc	0.1423	0.5072		$pS6K^{T389}$	$pERK^{T202/Y204}$	pc	0.0102	0.9623
$pGSK3b^{S9}$	$pERK^{T202/Y204}$	pc	0.2302	0.2791		$pGSK3b^{S9}$	$pERK^{T202/Y204}$	pc	0.2495	0.2397		$pGSK3b^{S9}$	$pERK^{T202/Y204}$	pc	0.3045	0.148

Figure 3 - figure supplement 1

1 nM to 10 nM

pAKT^{T308}

Source	Target	Interaction	Pearson r	p value
pAKT^{S473}	pAKT^{T308}	pc	0.4041	0.0502
pAKT^{S473}	pS6K^{T389}	pc	0.3085	0.1425
pAKT^{S473}	pGSK3b^{S9}	pc	0.3549	0.0888
pAKT^{S473}	pERK$^{T202/Y204}$	pc	-0.125	0.5607
pAKT^{T308}	pS6K^{T389}	pc	-0.3638	0.0805
pAKT^{T308}	pGSK3b^{S9}	pc	-0.3708	0.0745
pAKT^{T308}	pERK$^{T202/Y204}$	pc	-0.5323	0.0074
pS6K^{T389}	pGSK3b^{S9}	pc	0.9363	<0.0001
pS6K^{T389}	pERK$^{T202/Y204}$	pc	0.1423	0.5072
pGSK3b^{S9}	pERK$^{T202/Y204}$	pc	0.2495	0.2397

pAKT^{S473}

Source	Target	Interaction	Pearson r	p value
pAKT^{S473}	pAKT^{T308}	pc	0.6505	0.0006
pAKT^{S473}	pS6K^{T389}	pc	-0.03638	0.866
pAKT^{S473}	pGSK3b^{S9}	pc	-0.0008821	0.9967
pAKT^{S473}	pERK$^{T202/Y204}$	pc	-0.3459	0.0978
pAKT^{T308}	pS6K^{T389}	pc	0.4316	0.0352
pAKT^{T308}	pGSK3b^{S9}	pc	0.4546	0.0256
pAKT^{T308}	pERK$^{T202/Y204}$	pc	-0.3916	0.0584
pS6K^{T389}	pGSK3b^{S9}	pc	0.9363	<0.0001
pS6K^{T389}	pERK$^{T202/Y204}$	pc	0.1423	0.5072
pGSK3b^{S9}	pERK$^{T202/Y204}$	pc	0.2495	0.2397

pGSK3b^{S9}

Source	Target	Interaction	Pearson r	p value
pAKT^{S473}	pAKT^{T308}	pc	0.8408	<0.0001
pAKT^{S473}	pS6K^{T389}	pc	0.3085	0.1425
pAKT^{S473}	pGSK3b^{S9}	pc	0.4986	0.0131
pAKT^{S473}	pERK$^{T202/Y204}$	pc	-0.125	0.5607
pAKT^{T308}	pS6K^{T389}	pc	0.4316	0.0352
pAKT^{T308}	pGSK3b^{S9}	pc	0.3738	0.0719
pAKT^{T308}	pERK$^{T202/Y204}$	pc	-0.3916	0.0584
pS6K^{T389}	pGSK3b^{S9}	pc	0.4214	0.0403
pS6K^{T389}	pERK$^{T202/Y204}$	pc	0.1423	0.5072
pGSK3b^{S9}	pERK$^{T202/Y204}$	pc	0.5389	0.0066

pS6K^{T389}

Source	Target	Interaction	Pearson r	p value
pAKT^{S473}	pAKT^{T308}	pc	0.8408	<0.0001
pAKT^{S473}	pS6K^{T389}	pc	0.3303	0.115
pAKT^{S473}	pGSK3b^{S9}	pc	0.3549	0.0888
pAKT^{S473}	pERK$^{T202/Y204}$	pc	-0.125	0.5607
pAKT^{T308}	pS6K^{T389}	pc	0.2266	0.2871
pAKT^{T308}	pGSK3b^{S9}	pc	0.4546	0.0256
pAKT^{T308}	pERK$^{T202/Y204}$	pc	-0.3916	0.0584
pS6K^{T389}	pGSK3b^{S9}	pc	0.7648	<0.0001
pS6K^{T389}	pERK$^{T202/Y204}$	pc	0.4734	0.0195
pGSK3b^{S9}	pERK$^{T202/Y204}$	pc	0.2495	0.2397

pERK$^{T202/Y204}$

Source	Target	Interaction	Pearson r	p value
pAKT^{S473}	pAKT^{T308}	pc	0.8408	<0.0001
pAKT^{S473}	pS6K^{T389}	pc	0.3085	0.1425
pAKT^{S473}	pGSK3b^{S9}	pc	0.3549	0.0888
pAKT^{S473}	pERK$^{T202/Y204}$	pc	-0.07615	0.7236
pAKT^{T308}	pS6K^{T389}	pc	0.4316	0.0352
pAKT^{T308}	pGSK3b^{S9}	pc	0.4546	0.0256
pAKT^{T308}	pERK$^{T202/Y204}$	pc	-0.2724	0.1979
pS6K^{T389}	pGSK3b^{S9}	pc	0.9363	<0.0001
pS6K^{T389}	pERK$^{T202/Y204}$	pc	-0.0742	0.7304
pGSK3b^{S9}	pERK$^{T202/Y204}$	pc	-0.05353	0.8038

pAKT$^{T308 \text{ and } S473}$

Source	Target	Interaction	Pearson r	p value
pAKT^{S473}	pAKT^{T308}	pc	0.8451	<0.0001
pAKT^{S473}	pS6K^{T389}	pc	-0.03638	0.866
pAKT^{S473}	pGSK3b^{S9}	pc	-0.0008821	0.9967
pAKT^{S473}	pERK$^{T202/Y204}$	pc	-0.3459	0.0978
pAKT^{T308}	pS6K^{T389}	pc	-0.3638	0.0805
pAKT^{T308}	pGSK3b^{S9}	pc	-0.3708	0.0745
pAKT^{T308}	pERK$^{T202/Y204}$	pc	-0.5323	0.0074
pS6K^{T389}	pGSK3b^{S9}	pc	0.9363	<0.0001
pS6K^{T389}	pERK$^{T202/Y204}$	pc	0.1423	0.5072
pGSK3b^{S9}	pERK$^{T202/Y204}$	pc	0.2495	0.2397

0.1 nM to 10 nM

pAKT^{T308}

Source	Target	Interaction	Pearson r	p value
pAKT^{S473}	pAKT^{T308}	pc	0.1104	0.6074
pAKT^{S473}	pS6K^{T389}	pc	0.5068	0.0115
pAKT^{S473}	pGSK3b^{S9}	pc	0.4997	0.0129
pAKT^{S473}	pERK$^{T202/Y204}$	pc	-0.1768	0.4086
pAKT^{T308}	pS6K^{T389}	pc	-0.3745	0.0714
pAKT^{T308}	pGSK3b^{S9}	pc	-0.3197	0.1278
pAKT^{T308}	pERK$^{T202/Y204}$	pc	-0.7063	0.0001
pS6K^{T389}	pGSK3b^{S9}	pc	0.6607	0.0004
pS6K^{T389}	pERK$^{T202/Y204}$	pc	0.588	0.0025
pGSK3b^{S9}	pERK$^{T202/Y204}$	pc	0.2302	0.2791

pAKT^{S473}

Source	Target	Interaction	Pearson r	p value
pAKT^{S473}	pAKT^{T308}	pc	0.5919	0.0023
pAKT^{S473}	pS6K^{T389}	pc	0.04006	0.8526
pAKT^{S473}	pGSK3b^{S9}	pc	-0.1941	0.3633
pAKT^{S473}	pERK$^{T202/Y204}$	pc	-0.4395	0.0317
pAKT^{T308}	pS6K^{T389}	pc	0.3899	0.0596
pAKT^{T308}	pGSK3b^{S9}	pc	0.2441	0.2503
pAKT^{T308}	pERK$^{T202/Y204}$	pc	-0.2486	0.2415
pS6K^{T389}	pGSK3b^{S9}	pc	0.6607	0.0004
pS6K^{T389}	pERK$^{T202/Y204}$	pc	0.588	0.0025
pGSK3b^{S9}	pERK$^{T202/Y204}$	pc	0.2302	0.2791

pGSK3b^{S9}

Source	Target	Interaction	Pearson r	p value
pAKT^{S473}	pAKT^{T308}	pc	0.8732	<0.0001
pAKT^{S473}	pS6K^{T389}	pc	0.5068	0.0115
pAKT^{S473}	pGSK3b^{S9}	pc	0.2465	0.2456
pAKT^{S473}	pERK$^{T202/Y204}$	pc	-0.1768	0.4086
pAKT^{T308}	pS6K^{T389}	pc	0.3899	0.0596
pAKT^{T308}	pGSK3b^{S9}	pc	0.3001	0.1542
pAKT^{T308}	pERK$^{T202/Y204}$	pc	-0.2486	0.2415
pS6K^{T389}	pGSK3b^{S9}	pc	0.6221	0.0012
pS6K^{T389}	pERK$^{T202/Y204}$	pc	0.588	0.0025
pGSK3b^{S9}	pERK$^{T202/Y204}$	pc	0.4621	0.023

pS6K^{T389}

Source	Target	Interaction	Pearson r	p value
pAKT^{S473}	pAKT^{T308}	pc	0.8732	<0.0001
pAKT^{S473}	pS6K^{T389}	pc	0.3486	0.095
pAKT^{S473}	pGSK3b^{S9}	pc	0.4997	0.0129
pAKT^{S473}	pERK$^{T202/Y204}$	pc	-0.1768	0.4086
pAKT^{T308}	pS6K^{T389}	pc	0.3439	0.0998
pAKT^{T308}	pGSK3b^{S9}	pc	0.2441	0.2503
pAKT^{T308}	pERK$^{T202/Y204}$	pc	-0.2486	-0.2486
pS6K^{T389}	pGSK3b^{S9}	pc	0.3532	0.0904
pS6K^{T389}	pERK$^{T202/Y204}$	pc	0.6653	0.0004
pGSK3b^{S9}	pERK$^{T202/Y204}$	pc	0.2302	0.2791

pERK$^{T202/Y204}$

Source	Target	Interaction	Pearson r	p value
pAKT^{S473}	pAKT^{T308}	pc	0.8732	<0.0001
pAKT^{S473}	pS6K^{T389}	pc	0.5068	0.0115
pAKT^{S473}	pGSK3b^{S9}	pc	0.4997	0.0129
pAKT^{S473}	pERK$^{T202/Y204}$	pc	-0.3829	0.0648
pAKT^{T308}	pS6K^{T389}	pc	0.3899	0.0596
pAKT^{T308}	pGSK3b^{S9}	pc	0.2441	0.2503
pAKT^{T308}	pERK$^{T202/Y204}$	pc	-0.3417	0.1022
pS6K^{T389}	pGSK3b^{S9}	pc	0.6607	0.0004
pS6K^{T389}	pERK$^{T202/Y204}$	pc	-0.06901	0.7486
pGSK3b^{S9}	pERK$^{T202/Y204}$	pc	0.04658	0.8289

pAKT$^{T308 \text{ and } S473}$

Source	Target	Interaction	Pearson r	p value
pAKT^{S473}	pAKT^{T308}	pc	0.8451	<0.0001
pAKT^{S473}	pS6K^{T389}	pc	0.04006	0.8526
pAKT^{S473}	pGSK3b^{S9}	pc	-0.1941	0.3633
pAKT^{S473}	pERK$^{T202/Y204}$	pc	-0.4395	0.0317
pAKT^{T308}	pS6K^{T389}	pc	-0.3745	0.0714
pAKT^{T308}	pGSK3b^{S9}	pc	-0.3197	0.1278
pAKT^{T308}	pERK$^{T202/Y204}$	pc	-0.7063	0.0001
pS6K^{T389}	pGSK3b^{S9}	pc	0.6607	0.0004
pS6K^{T389}	pERK$^{T202/Y204}$	pc	0.588	0.0025
pGSK3b^{S9}	pERK$^{T202/Y204}$	pc	0.2302	0.2791

Figure 3 - figure supplement 2

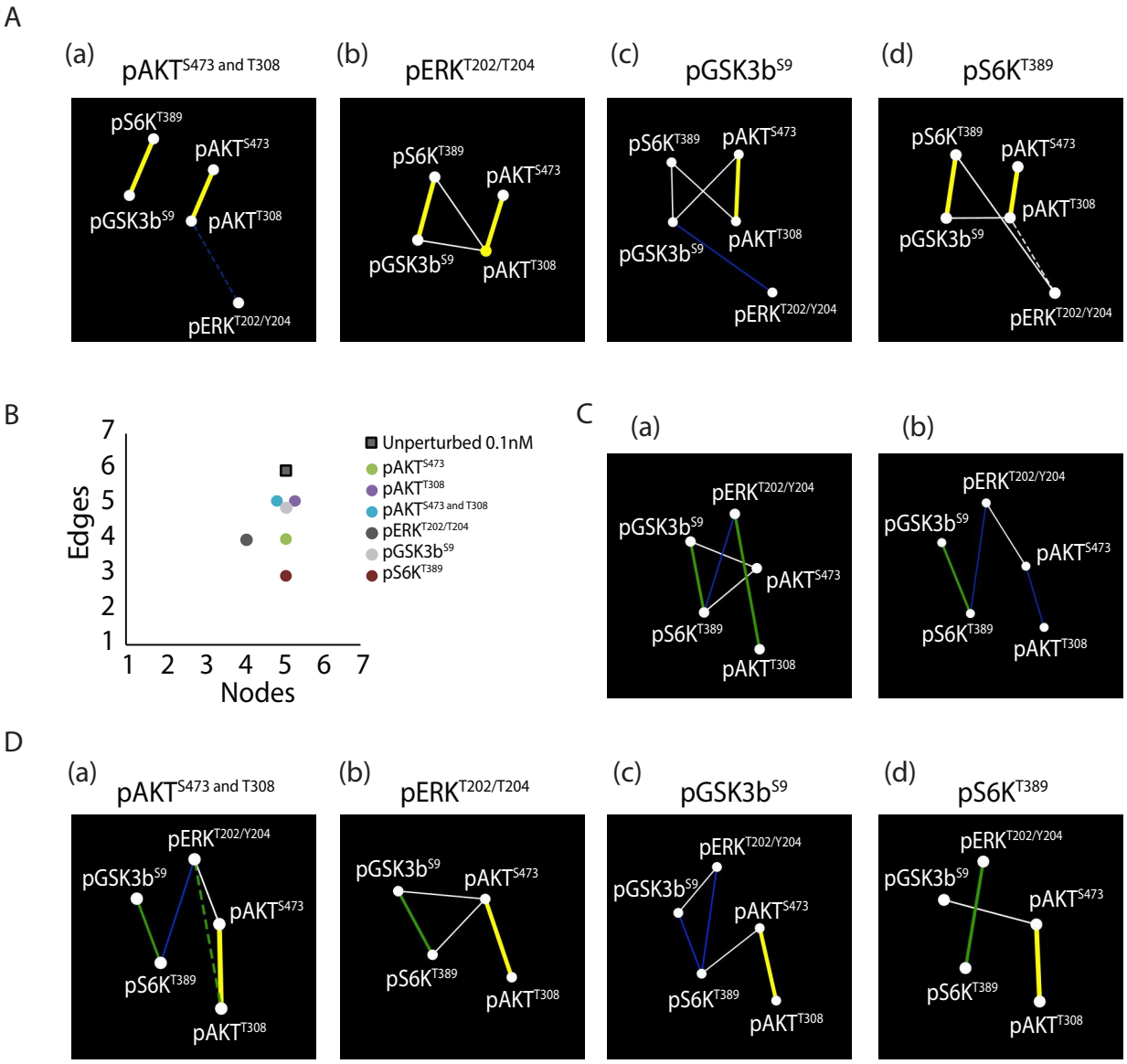

Figure 3 - figure supplement 3

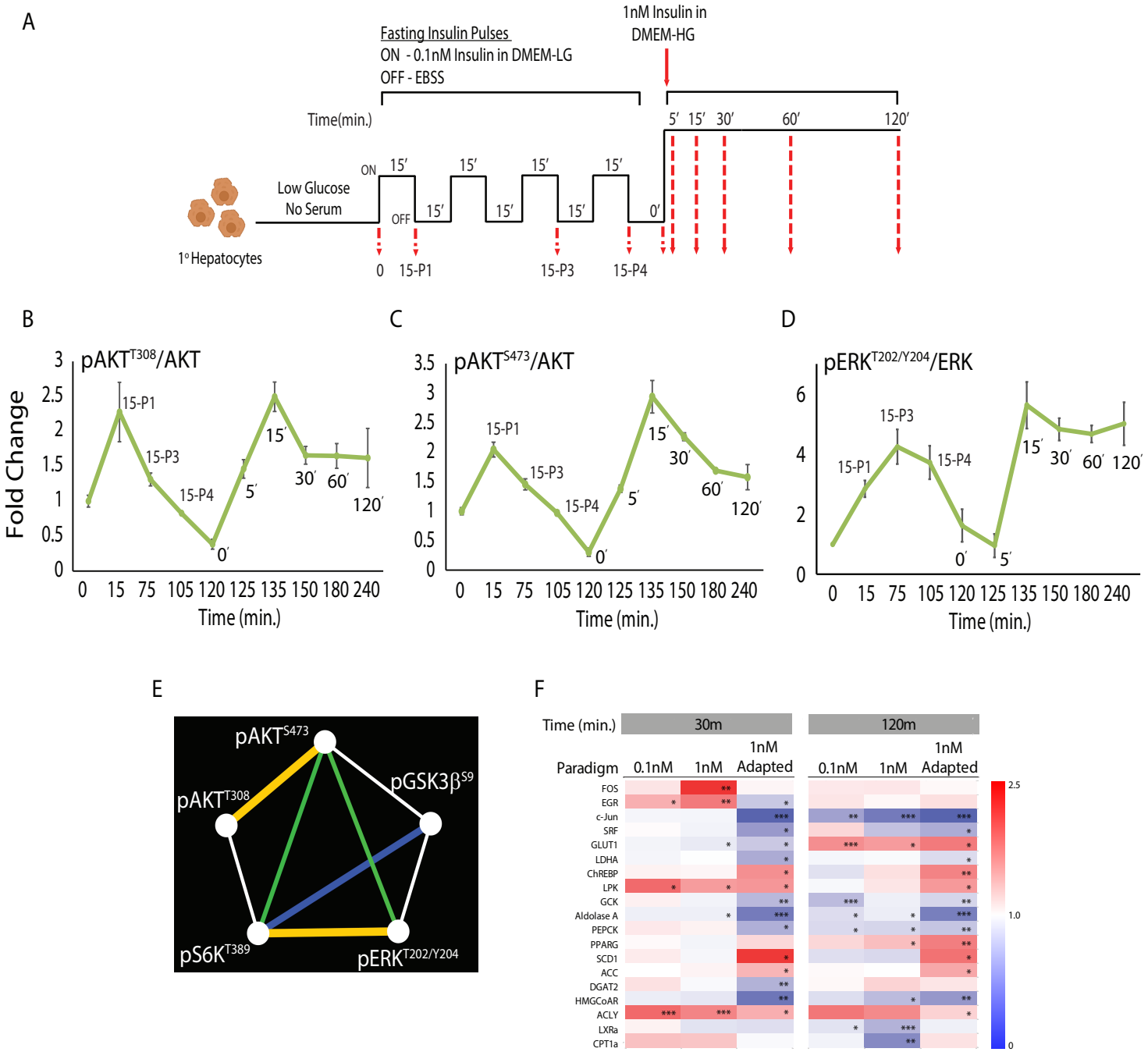
A
Fasting Insulin Pulses
ON - 0.1nM Insulin in DMEM-LG
OFF - EBSS
1nM Insulin in DMEM-HG
Time(min.)
5′ 15′ 30′ 60′ 120′
ON 15′ 15′ 15′ 15′ 0′
OFF 15′ 15′ 15′
Low Glucose
No Serum
1°Hepatocytes
0 15-P1 15-P3 15-P4
B
pAKT^T308/AKT
Fold Change
15-P1 15-P3 15-P4 0′ 5′ 15′ 30′ 60′ 120′
0 15 75 105 120 125 135 150 180 240
Time (min.)
C
pAKT^S473/AKT
15-P1 15-P3 15-P4 0′ 5′ 15′ 30′ 60′ 120′
0 15 75 105 120 125 135 150 180 240
Time (min.)
D
pERK^T202/Y204/ERK
15-P1 15-P3 15-P4 0′ 5′ 15′ 30′ 60′ 120′
0 15 75 105 120 125 135 150 180 240
Time (min.)
E
pAKT^S473
pAKT^T308
pGSK3β^S9
pS6K^T389
pERK^T202/Y204
F
Time (min.)
30m
120m
Paradigm
0.1nM
1nM
1nM Adapted
FOS
EGR
c-Jun
SRF
GLUT1
LDHA
ChREBP
LPK
GCK
Aldolase A
PEPCK
PPARG
SCD1
ACC
DGAT2
HMGCoAR
ACLY
LXRa
CPT1a
2.5
1.0
0

Figure 4

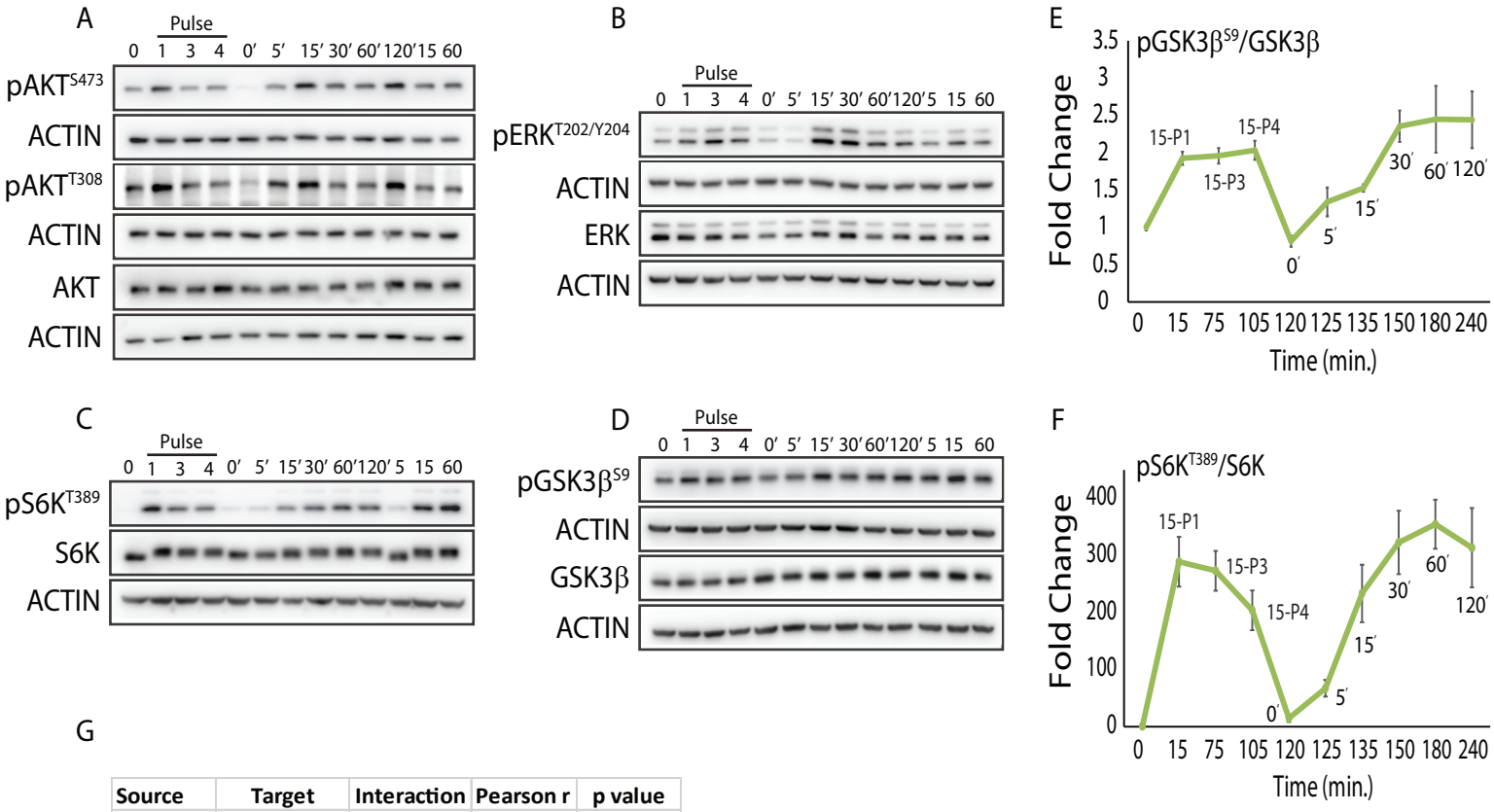

G

Source	Target	Interaction	Pearson r	p value
pAKT^{S473}	pAKT^{T308}	pc	0.8762	0.0001
pAKT^{S473}	pS6K^{T389}	pc	0.6081	0.0074
pAKT^{S473}	pGSK3b^{S9}	pc	0.4746	0.0466
pAKT^{S473}	pERK$^{T202/Y204}$	pc	0.6549	0.0032
pAKT^{T308}	pS6K^{T389}	pc	0.5071	0.0317
pAKT^{T308}	pGSK3b^{S9}	pc	0.419	0.0835
pAKT^{T308}	pERK$^{T202/Y204}$	pc	0.4368	0.1908
pS6K^{T389}	pGSK3b^{S9}	pc	0.7692	0.0002
pS6K^{T389}	pERK$^{T202/Y204}$	pc	0.8068	0.0001
pGSK3b^{S9}	pERK$^{T202/Y204}$	pc	0.4866	0.0406

Figure 4 - figure supplement 1

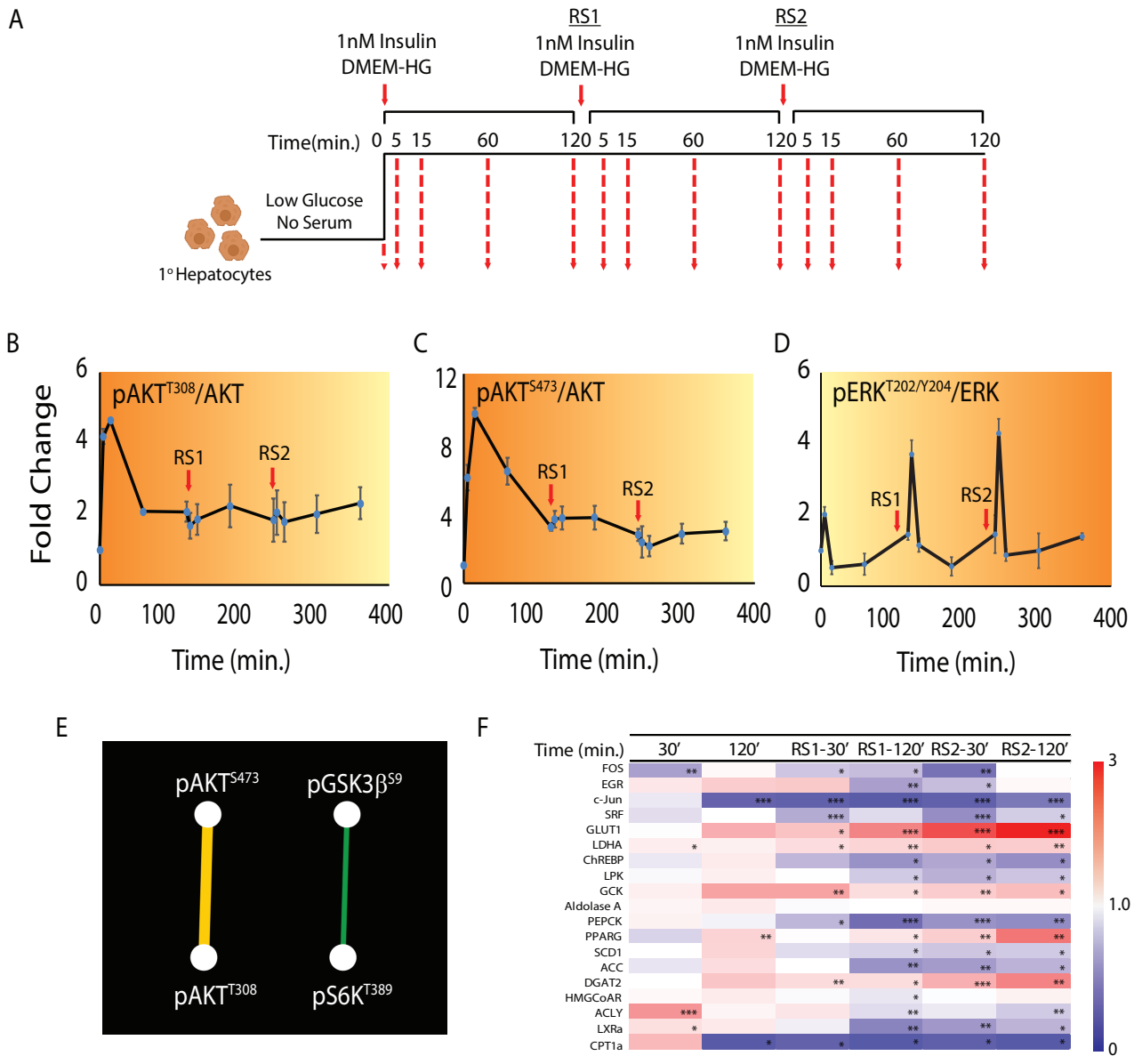
A
1nM Insulin
DMEM-HG
RS1
1nM Insulin
DMEM-HG
RS2
1nM Insulin
DMEM-HG
Time(min.) 0 5 15 60 120 5 15 60 120 5 15 60 120
Low Glucose
No Serum
1° Hepatocytes
B
pAKTT308/AKT
Fold Change
RS1
RS2
Time (min.)
C
pAKTS473/AKT
RS1
RS2
Time (min.)
D
pERKT202/Y204/ERK
RS1
RS2
Time (min.)
E
pAKTS473
pGSK3βS9
pAKTT308
pS6KT389
F
Time (min.)
30′
120′
RS1-30′
RS1-120′
RS2-30′
RS2-120′
FOS
EGR
c-Jun
SRF
GLUT1
LDHA
ChREBP
LPK
GCK
Aldolase A
PEPCK
PPARG
SCD1
ACC
DGAT2
HMGCoAR
ACLY
LXRa
CPT1a
3
1.0
0

Figure 5

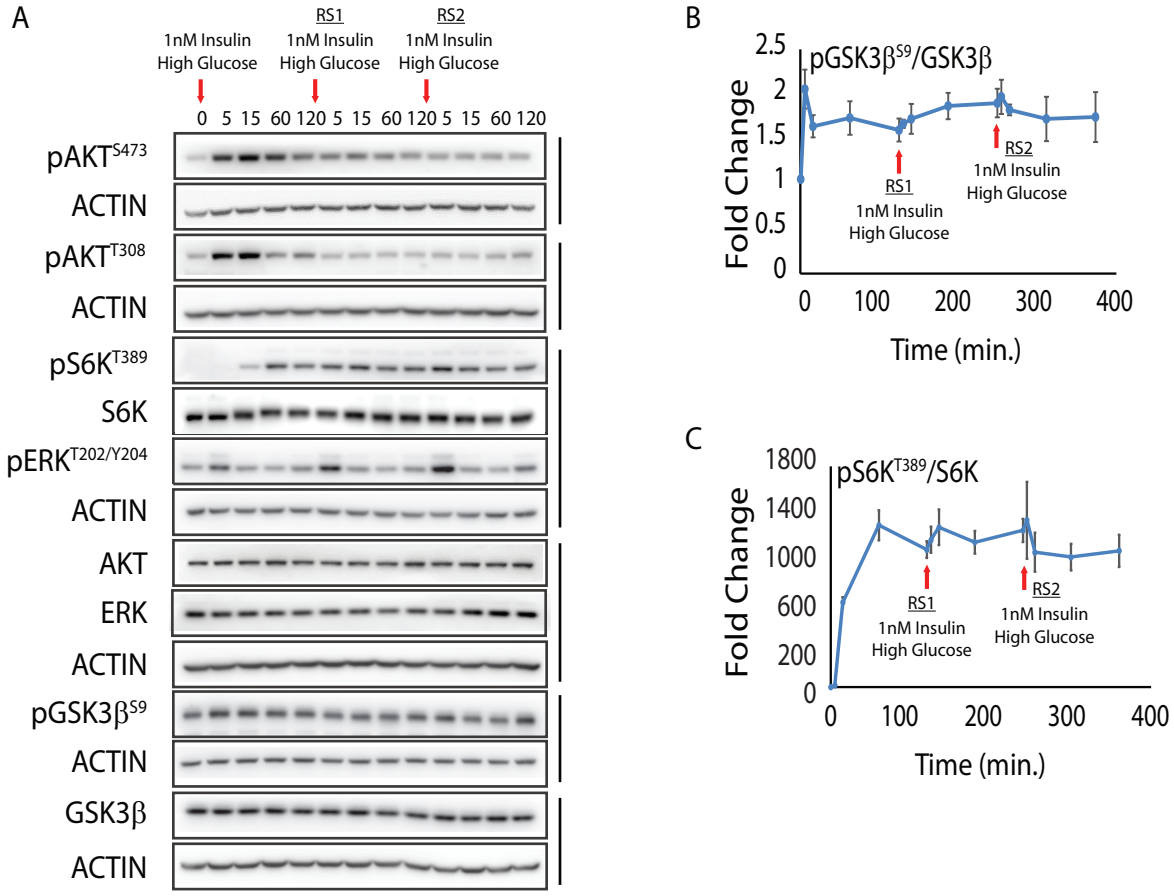

C

Source	Target	Interaction	Pearson r	p value
pAKT^{S473}	pAKT^{T308}	pc	0.7641	0.0001
pAKT^{S473}	pS6K^{T389}	pc	-0.05917	0.72
pAKT^{S473}	pGSK3b^{S9}	pc	0.1098	0.5059
pAKT^{S473}	pERK$^{T202/Y204}$	pc	-0.2116	0.1959
pAKT^{T308}	pS6K^{T389}	pc	-0.246	0.1312
pAKT^{T308}	pGSK3b^{S9}	pc	0.03422	0.8361
pAKT^{T308}	pERK$^{T202/Y204}$	pc	-0.1189	0.471
pS6K^{T389}	pGSK3b^{S9}	pc	0.3354	0.0369
pS6K^{T389}	pERK$^{T202/Y204}$	pc	0.157	0.3399
pGSK3b^{S9}	pERK$^{T202/Y204}$	pc	0.2648	0.1033

Figure 5 - figure supplement 1